Single nucleus RNA sequencing reveals glial cell type-specific responses to ischemic stroke

Daniel Bormann[1,2], Michael Knoflach[3,4], Emilia Poreba[5], Christian J. Riedl[6], Giulia Testa[6], Cyrille Orset[7,8], Anthony Levilly[7,8], Andreá Cottereau[7,8], Philipp Jauk[6,9], Simon Hametner[6], Bahar Golabi[5], Dragan Copic[1,2,10], Katharina Klas[1,2], Martin Direder[1,2,11], Hannes Kühtreiber[1,2], Melanie Salek[1,2], Stephanie zur Nedden[12], Gabriele Baier-Bitterlich[12], Stefan Kiechl[3,4], Carmen Haider[6], Verena Endmayr[6], Romana Höftberger[6], Hendrik J. Ankersmit[1,2]*, Michael Mildner[5]*

[1] Applied Immunology Laboratory, Department of Thoracic Surgery, Medical University of Vienna, 1090 Vienna, Austria

[2]Aposcience AG, 1200 Vienna, Austria

[3]Department of Neurology, Medical University of Innsbruck, Anichstraße 35, 6020 Innsbruck, Austria

[4] VASCage, Research Centre on Vascular Ageing and Stroke, 6020 Innsbruck, Austria

[5]Department of Dermatology, Medical University of Vienna, 1090 Vienna, Austria

[6]Division of Neuropathology and Neurochemistry, Department of Neurology, Medical University of Vienna, 1090 Vienna, Austria

[7]Normandie University, UNICAEN, ESR3P, INSERM UMR-S U1237, Physiopathology and Imaging of Neurological Disorders (PhIND), GIP Cyceron, Institut Blood and Brain @ Caen-Normandie (BB@C), Caen, France

[8]Department of Clinical Research, Caen-Normandie University Hospital, Caen, France

[9]Center for Medical Physics and Biomedical Engineering, Medical University of Vienna, 1090 Vienna, Austria

[10]Division of Nephrology and Dialysis, Department of Internal Medicine III, Medical University of Vienna, 1090 Vienna, Austria.

[11]Department of Orthopedics and Trauma Surgery, Medical University of Vienna, 1090 Vienna, Austria

[12]Institute of Neurobiochemistry, CCB-Biocenter, Medical University of Innsbruck, 6020 Innsbruck, Austria

*: contributed equally

Correspondence to:

Michael Mildner, PhD

Department of Dermatology, Medical University of Vienna

Lazarettgasse 14, 1090 Vienna, Austria

phone: +43-(0)1-40400-73507

e-mail: michael.mildner@meduniwien.ac.at

or

Hendrik Jan Ankersmit, MD, MBA

Applied Immunology Laboratory, Department of Thoracic Surgery, Medical University of Vienna, Waehringer Guertel 18-20, 1090 Vienna, Austria.

e-mail: hendrik.ankersmit@meduniwien.ac.at

Abstract

Reactive neuroglia critically shape the brain´s response to ischemic stroke. However, their phenotypic heterogeneity impedes a holistic understanding of the cellular composition and microenvironment of the early ischemic lesion. Here we generated a single cell resolution transcriptomics dataset of the injured brain during the acute recovery from permanent middle cerebral artery occlusion. This approach unveiled infarction and subtype specific molecular signatures in oligodendrocyte lineage cells and astrocytes, which ranged among the most transcriptionally perturbed cell types in our dataset. Specifically, we characterized and compared infarction restricted proliferating oligodendrocyte precursor cells (OPCs), mature oligodendrocytes and heterogeneous reactive astrocyte populations. Our analyses unveiled unexpected commonalities in the transcriptional response of oligodendrocyte lineage cells and astrocytes to ischemic injury. Moreover, OPCs and reactive astrocytes were involved in a shared immuno-glial cross talk with stroke specific myeloid cells. *In situ,* osteopontin positive myeloid cells accumulated in close proximity to proliferating OPCs and reactive astrocytes, which expressed the osteopontin receptor CD44, within the perilesional zone specifically. *In vitro,* osteopontin increased the migratory capacity of OPCs. Collectively, our study highlights molecular cross talk events which might govern the cellular composition and microenvironment of infarcted brain tissue in the early stages of recovery.

Keywords

Single nucleus RNA sequencing (snRNAseq), ischemic stroke, cerebral ischemia, oligodendrocytes, oligodendrocyte precursor cells, astrocytes, myeloid cells

Introduction

The brain is among the most metabolically costly mammalian organs [72] and hence particularly vulnerable to ischemia [25]. The sudden deprivation of oxygen and substrate availability in the brain parenchyma triggers a cascade of complex pathophysiological events, culminating in the loss of neural tissue and lasting neurological dysfunction [17, 25]. In humans, this oxygen and substrate deprivation is most often caused by an acute, critical reduction of cerebral blood flow, due to the occlusion of large cerebral arteries, the most common cause of ischemic stroke [17].

Ischemic stroke is the second leading cause of disability and death worldwide and the global disease burden of ischemic stroke has been predicted to increase [28]. Apart from supportive care, all currently approved acute treatment strategies, that is thrombolysis and mechanical thrombectomy, aim to reinstate cerebral blood flow and are generally only effective when initiated within a timeframe of under 24h after stroke onset [76]. Therefore, the lack of treatment strategies directed at neural tissue regeneration constitute an important unmet therapeutic need. Nevertheless, spontaneous, albeit typically incomplete, regain of function after stroke is common and already observable within the acute phase of recovery, ranging from approximately 1 to 7 days [9, 20]. Numerous endogenous recovery mechanisms of the injured CNS have thus been postulated [82].

Cerebral ischemia triggers a breakdown of neurovascular unit (NVU) integrity, inflammation, neuronal cell death and white matter injury [43, 79]. This tissue damage is met with pronounced transcriptional, biochemical and morphological changes in glial cells, including reactive astrogliosis and early remyelination [43, 101]. However, current knowledge on the phenotypic heterogeneity within each reactive cell type and their precise interactions during the acute recovery from cerebral ischemic injury is still limited. Single-cell sequencing technologies have proven to be highly effective in addressing the challenges posed by the complex cellular heterogeneity of the CNS, in health and disease [75]. Arguably, most efforts in dissecting single cell transcriptomes after cerebral ischemia have been directed at immune and vascular cells [10, 16, 49, 58, 87, 105]. Thus far, particularly few studies have captured sufficient oligodendrocyte linage cells to identify robust subtype specific transcriptional changes following stroke [35, 45]. Moreover, extensive transcriptional comparisons between reactivate

astrocytes and oligodendrocyte lineage cells in response to cerebral ischemia are still lacking.

Here we generated a large-scale single nucleus transcriptome dataset of the brain´s acute response to ischemic stroke. We dissected subtype specific transcriptional signatures of stroke reactive neuroglia, compared subtype specific astrocyte and oligodendrocyte lineage cell responses and contrasted these changes with gene expressional profiles found in other CNS injuries. Our study highlights common immuno-glial molecular crosstalk events between myeloid cells, oligodendrocyte precursor cells (OPC) and reactive astrocytes, which might shape the cellular composition and microenvironment during early post ischemic neural regeneration.

Materials and Methods

Study approval/ Ethics statement

All *in vivo* animal experiments were performed in accordance with the French ethical law (Decree 2013-118) and the European Union directive (2010/63/EU). The protocol was submitted for ethic approval to the French Ministry of Research and the ethical committee (CENOMEXA – registered under the reference CENOMEXA-C2EA – 54) and received the agreement number #36435. The experiments have been reported in compliance with ARRIVE 2.0 guidelines. Archived human biopsy derived brain tissue material was used in agreement with the Medical University of Vienna ethics committee votes: EK1636/2019, EK1454/2018).

Animal husbandry

All experiments were performed on male Wistar rats (6 weeks at receipt, ± 30g, Janvier Lab, Le Genest-Sainte-Isle). Throughout the experiments, animals were maintained in standard husbandry conditions (temperature: 22 ± 2°C; hygrometry: 50 ± 20%), under reversed light-dark cycle (light from 08:00 to 20:00), with ad libitum access to water and food. Animals were housed at two per cage in the presence of enrichment.

Permanent Middle cerebral artery occlusion (MCAO) model

Cerebral ischemia was induced by intraluminal occlusion of the middle cerebral artery (MCAO). Briefly, rats were anesthetized with isoflurane (2-2.5%) in a mixture of O_2/N_2O (30%/70%). During surgery, animal temperature was monitored with a rectal probe and

was maintained at 37.5 °C with a heating pad. To induce permanent occlusion of the middle cerebral artery (MCA) a silicone rubber-coated monofilament (size 5-0, diameter 0.15mm, length 30 mm; diameter with coating 0.38 +/- 0.02 mm; Doccol, Sharon, MA, USA) was introduced into the lumen of the right external carotid, advanced through the internal carotid, and gently pushed up to the origin of the MCA. After wound stitching, the rats were returned to their home cage after receiving analgesics (buprenorphine, 0.05 mg/kg, subcutaneously). In Sham operated animals all experimental procedures were performed except for the filament insertion.

Magnetic Resonance Imaging (MRI)

To confirm successful induction of ischemic stroke and determine the anatomical localization of the stroke lesion MRI was carried out 48h after stroke onset, on a Pharmascan 7T MRI system, using surface coils (Bruker, Germany), following a previously described approach [5]. For lesion volume evaluation, T2-weighted images were acquired using a multislice multiecho sequence: TE/TR 33 ms/2500 ms. Lesion sizes were quantified on these images using ImageJ software. Lesion volumes were determined by a trained investigator blinded to condition and are expressed in mm^3.

Tissue sampling

After completion of MRI studies, animals were sacrificed via sharp blade decapitation in isoflurane anaesthesia, as described above. For single nucleus RNA sequencing studies whole brains were extracted and swiftly cut into standardized coronal sections using an adult rat brain slicer matrix (BSRAS003-1, with 3mm coronal section intervals, Zivic Instruments, Pittsburgh, PA, USA) and hemispheres were separated. Coronal slices, separated by hemisphere were then immediately snap frozen in liquid nitrogen and stored at –80°C until further transport on dry ice.

For Immunofluorescence assays anesthetized animals were transcardially perfused with DPBS, followed by perfusion with 4%PFA in DPBS, brains were harvested whole, further post fixed overnight in 4%PFA in DPBS, and washed three times in DPBS. Brains were then stored in DPBS with 0.05% Sodium Azide at 4°C until further processing. To match the anatomical regions used for snRNAseq assays, brains where cut into standardized coronal sections using the same adult rat brain slicer matrix (BSRAS003-1), described above. After cutting, brain tissue was dehydrated and embedded in paraffin.

Single nuclei preparation

Single nuclei suspensions were prepared as previously described [15]. Briefly, frozen brain sections were thawed in ice cold Nuclei Extraction Buffer (cat#: 130-128-024, Miltenyi) in gentleMACS™ C-Tubes (cat#: 130-093-237, Miltenyi Biotec, Bergisch Gladbach, Germany), followed by automated gentleMACS™ Octo dissociation (cat#: 130-096-427, Miltenyi) using program: 4C_nuclei_1 and a further 6 min incubation on ice. Suspensions were then strained into 15 ml polypropylene tubes (cat#: 430766, Corning, Corning, NY, USA) over 70 µm strainers (cat#: 542070, Greiner Bio-One International GmbH, Kremsmünster, Austria), 4 ml of ice cold nuclei extraction buffer were added, followed by centrifugation at 500 g, 4°C, for 5 min on a swing bucket centrifuge (Allegra X-12R, Beckman Coulter, Brea, CA, USA). Supernatant was decanted and the pellet was resuspended in 0.25% (vol/vol) Glycerol (cat#: G5516, Sigma Aldrich) and 5% (wt/vol) bovine serum albumin (BSA) (cat#A-9647, Sigma Aldrich) in Dulbecco's phosphate-buffered saline (DPBS) (cat# 14190-94, Gibco, ThermoFisher Scientific, Waltham, MA, USA)) (=nucleus wash buffer (NWB1), buffer composition derived from [62]. Suspensions were then strained through 40 µm strainers (cat#: 352340, Falcon®, Corning) and centrifuged at a swing bucket centrifuge at 500 g, 4°C for 5 min. The pellet containing nuclei and debris was resuspended in a Tricin-KOH buffered (pH 7.8), 10% Iodixanol solution (10% Iodixanol (OptiPrep™, cat#: 7820, STEMCELL Technologies, Vancouver, BC, Canada), 25 mM KCl (cat#: 60142), 5 mM MgCl2 (cat#: M1028), 20 mM Tricin (cat#: T0377) KOH (cat#: 484016), 200 mM Sucrose (cat#: S0389) , all from Sigma Aldrich) and gently layered on top of a 20% Iodixanol gradient cushion (20% Iodixanol, 150mM Sucrose, 25 mM KCl, 5 mM MgCl2, 20 mM Tricine-KOH, pH 7.8) in 14x89 mm thin wall polypropylene centrifuge tubes (cat#: 344059, Beckman Coulter, Brea, CA, USA). An Optima L-80 Ultracentrifuge (serial#: Col94H18, Beckman Coulter), with swing bucket SW41 Ti cartridges, precooled to 4°C was used for gradient centrifugation at 10000g, for 30 min, with maximal acceleration and no brake. Following centrifugation, debris fractions were discarded and the purified nuclei pellet was resuspended in ice cold NWB1 and strained over 30 µm strainers (cat#: 130-098-458, Miltenyi). The suspension was centrifuged at a swing bucket centrifuge at 500g, 4°C, for 5 min, supernatant was discarded and nuclei were resuspended in a solution of 3% BSA, 0.125% Glycerol, in DPBS (=NWB2). This washing step was repeated once. Finally, nuclei were resuspended in a solution of 1.5% BSA in DPBS on ice. To obtain nuclei counts, nuclei

were stained using the Acridine Orange/Propidium Iodide (AO/PI) Cell Viability Kit (cat#: F23001, Logos Biosystems, Anyang-si, Gyeonggi-do, South Korea). Nuclei were counted as PI positive events using a LUNA-FL™ Dual Fluorescence Cell Counter (cat#: L20001 Logos Biosystems). The fraction of non lysed Acridine Orange + cells was <5% in all samples. All buffers used during nuclei purification were supplemented with 0.2 U/µl RiboLock RNase Inhibitor (cas#: EO0384, ThermoFisher Scientific, Waltham, MA, USA).

Single nucleus processing and library preparation

Processing of single nuclei suspensions was performed as previously described [15], using the Chromium™ Next GEM Single Cell 5' Kit v2 (PN-1000263, 10 × Genomics, Pleasanton, CA, USA), as per manufacturer´s protocols (CG000331 Rev D, 10 × Genomics). In brief, for Gel Beads-in-Emulsion (GEMs) generation we loaded nuclei onto Chromium™ Next GEM Chips K (PN- 1000286 ,10 × Genomics), aiming at a recovery of 10-12x10^3 nuclei per lane, followed by GEM reverse transcription (GEM-RT) and clean up. GEM-RT products were subjected to 14 cycle of cDNA amplification using 10X poly(dT) primers, followed by 10X 5' gene expression library construction. The Single Index Kit TT Set A (PN 1000215, 10X Genomics) was used for sample indexing during library construction. SPRIselect Reagent Kit (cat#: B23318, Beckman Coulter) beads were used for clean-up procedures, as per 10X protocols instructions. The quality of the obtained libraries was assessed using a DNA screen tape D5000 on a TapeStation 4150 (Agilent Technologies, Santa Clara, CA, USA) and cDNA was quantified using a Qubit 1xdsDNA HS assay kit (cat#: Q33231) on a QuBit 4.0 fluorometer (Invitrogen, ThermoFisher Scientific). Libraries with unique indices were then pooled in equimolar ratios before sequencing.

Sequencing, pre-processing and quality control:

Samples were sequenced paired-end, with dual indexing (read length 50bp) using a NovaSeq 6000 (Illumina, San Diego, CA, USA). All samples were processed on the same flow cell. Raw gene counts were obtained by demultiplexing and alignment of reads to the most current *rattus norvegicus* reference genome mRatBN7.2, using the Cellranger v.7.0.0 pipeline, including intronic reads in the count matrix to account for unspliced nuclear transcripts, as per developer's recommendations. Cellranger outputs were further processed utilizing R and R Studio (R version 4.2.2, The R Foundation, Vienna, Austria), using the below indicated packages. Unless otherwise stated, all

computational snRNAseq analyses were carried out within the environment of the Seurat package v.4.3.0 [39], as per developer's vignettes.

For each individual dataset UMI count matrices were generated and converted to Seurat Objects, preliminary normalization and variance stabilization was performed using the SCTransform, v2 regularization [21, 37], followed by PCA dimensionality reduction with 50 principal components, and graph-based clustering using the "RunUMAP" "FindNeighbors" and "FindClusters" commands.

Using the preliminary clustering information for each dataset, ambient RNA contamination was estimated and ambient RNA was removed using the SoupX v1.6.2 package [102], following developers vignettes. The decontaminated expression matrices were then further processed following the standard Seurat quality control pipeline. Briefly, nuclei with < 500 UMI counts, <250 or >5000 expressed genes and > 5% mitochondrial genes expressed, were removed from downstream analysis. Doublets were estimated and removed using the DoubletFinder v2.0.3 package [66], as per developers vignettes. All genes with less than 3 UMI counts per feature and all mitochondrial genes were removed from downstream analyses.

Dataset integration:

After the above described quality control pipeline, normalization and variance stabilization was performed for all individual datasets, utilizing SCTransform, with v2 regularization, with the percentage of mitochondrial reads "percent.mt" passed to the "vars.to.regress" argument. All datasets were then integrated using reciprocal PCA (RPCA) based integration. Briefly, the top 3000 highly variable genes were selected utilizing the "SelectIntegrationFeatures" function. The datasets were then prepared for integration using the "PrepSCTIntegration" function, dimensionality reduction was performed for all datasets using the "RunPCA" command and integration anchors were established using the "FindIntegrationAnchors" function, with RPCA reduction using the first 30 dimension and the "k.anchor" argument set to 10. All datasets were then integrated using the "IntegrateData" function, generating a single integrated, batch-corrected expression matrix, which was used for all further downstream analyses.

Clustering and subclustering of cell types:

The Seurat function "RunPCA" was used for principal component analysis (PCA) followed by UMAP (Uniform Manifold Approximation and Projection) dimensionality

reduction and Louvain clustering, using the "RunUMAP" "FindNeighbors" and "FindClusters" functions. For sub clustering analysis, the clusters of interest were subset, split by sample and normalization, variance stabilization and integration was reiterated with the same parameters as described above. Thereafter PCA, UMAP dimensionality reduction and Louvain clustering were reiterated on the reintegrated and pre-processed subset to derive sub clusters.

Differential gene expression analysis:

The MAST statistical framework [30] within Seurat's "FindAllMarkers" and "FindMarkers" functions was used for differentially expressed gene (DEG) calculations to identify cluster markers, and between group differences in gene expression, as previously described [15], with minor modifications. Briefly, only genes expressed in a minimum of 10% of nuclei in either tested group were considered. Log-normalized RNA-counts were used for DEG analyses. The number of UMIs and the percentage of mitochondrial reads, were passed to the "latent.vars" argument. For between group comparison we defined a $|\log_2\text{fold change} \geq 0.6|$ and Bonferroni-adjusted p-value < 0.05 as DEG thresholds.

Module score calculations:

Seurat's "AddModuleScore" function was used to calculate module scores, for previously published gene sets, for each nucleus. All gene sets used are described in detail in Suppl.data.file.1. Human and mouse gene symbols were converted to human orthologs using the gorth tool in gprofiler2 [51], before module score calculation. Estimation of cell cycle phases was conducted using Seurat's "CellCycleScoring" function, as per developer's vignettes.

Enrichment analysis

Enrichment analysis was performed as previously described [15]. Briefly, rat gene names of DEGs of interest were converted to human orthologs using the gorth tool in gprofiler2 and used as input for Enrichr [55]. We queried the gene set databases "GO Biological Process 2023", "GO Molecular Function 2023", "Reactome 2022" and "KEGG 2021 Human". Only enriched terms with Benjamini-Hochberg method adjusted p values of <0.05 were retained.

Cell trajectory based pseudotime inference analysis

We conducted pseudotime trajectory analyses on the oligodendrocyte lineage subset using Monocle3 v.1.3.1 [18, 93], following developer's vignettes. To this end we converted the fully processed Seurat subset into a CDS object using the "as.cell_data_set" and pre-processed the CDC object for subsequent analyses using the "estimate_size_factors" and "preprocess_cds" functions at default parameters and transferred the cell cluster annotations and UMAP cell embeddings from the original Seurat object. Trajectory graph construction and estimation of pseudotime was performed using the "learn_graph" and "order_cells" functions. The Moran's I test based function "graph_test" was used to identify genes, which expressions are correlated or anticorrelated in adjacent cells along the inferred pseudotime trajectory, that is genes which expression changes as a function of pseudotime. "Principal_graph" was passed to the neighbor_graph argument in the function, as indicated by the packages developers and the obtained dataframe was subset to genes with corresponding q-values <0.05 and morans I >0.05. Thereafter, we used the "find_gene_modles" function, which runs UMAP and subsequent Louvain community analyses to identify co-regulated gene modules, at a resolution of 0.01. For plotting, the aggregate gene expression of all genes within a respective model was generated using the "aggregate_gene_expression" function.

Inference of transcription factor activity

We used the R package decoupleR, as per developers vignettes to infer transcription factor (TF) activities [6]. Briefly, CollecTRIs´ rat regulon database was retrieved via Omnipath [94] using the "get_collectri" function. DecoupleR´s Univariate Linear Model (ulm) was run on normalized log-transformed RNA counts using the "run_ulm" function, to infer transcription factor activity scores for each nucleus. Inferred transcription factor activity scores were then aggregate for each cluster within each group and presented as heatmaps.

Cell-cell communication inference analysis

To infer potential cell-cell communication (CCC) events between cell-types we used the LIgand-receptor ANalysis frAmework (LIANA) v.0.1.12, following developer's vignettes [26, 94]. Using the "generate_homologs" function LIANA's consensus CCC resource entries were converted to *rattus norvegicus* ortholog gene symbols. The

functions “liana_wrap” and “liana aggregate” were used at default settings to infer ligand receptor pairs and obtain consensus ranks across all default CCC methods using Robust Rank Aggregation (RRA). Only predicted ligand receptor interactions with aggregate rank scores ≤0.05 were retained for subsequent analyses.

Visualization of bioinformatics data

The following R packages were used for data visualization: Seurat v.4.3.0, Monocle3, ggplot2 [98], EnhancedVolcano v.1.16.0 [12], UpSetR v.1.4.0 [22], scCustomize v.1.1.1 [63], SCPubr v. 2.0.1 [11], ComplexHeatmap v. 2.14.0 [34] and pheatmap v. 1.0.12 [52].

Human brain tissue samples

Archived formalin-fixed, paraffin-embedded (FFPE) biopsy samples from 4 patients, (1 male, 3 females, 33 to 60 years of age) were included. Samples were graded by trained neuropathologists as cerebral infarctions in the stage of macrophage resorption (Stage II) and pseudo cystic cavity formation (Stage III), in accordance with previously described histopathological classifications [67].

Immunofluorescence staining

For Immunofluorescence (IF) staining 5 µm thick rat coronal whole brain sections and 3 µm thick human FFPE tissue sections were cut from paraffin blocks. After deparaffinization, sections were blocked in 0,9% H_2O_2 in methanol for 10 min and washed three times in ddH_2O, followed by 40 min of heat induced epitope retrieval (HIER) using DAKO Target Retrieval Solution pH6, or pH9 (cat# S2369, S2367, DAKO - Agilent Technologies), in a Braun household food steamer. Section were allowed to cool for 20min at room temperature, washed thrice in DPBS, and incubated with 1% sodium borohydride (cat# 1063710100, Merck Millipore, Burlington, MA, USA) in DPBS for 3 minutes to quench autofluoresence, followed by 3 washes in ddH2O and 3 washes in DPBS. Sections were then blocked and permeabilized in protein-blocking buffer (DPBS with 2% BSA, 10% fish gelatin (cat#: G7041, Sigma-Aldrich), 0.2% Triton-X (cat# T9284, Sigma-Aldrich)) for 30 min at room temperature. For some staining’s we directly labelled primary antibodies using FlexAble CoraLite® Plus Antibody Labeling Kits (Proteintech, Rosemont, IL, USA), as per manufacturer’s instructions. To colocalize antigens in tissue sections using primary antibodies derived from the same host species (all rabbit derived) we used the following approach. Tissue

sections were incubated with the first primary antibody for 18 h at 4°C, washed three times in DPBS and incubated with an appropriate secondary antibody for 1h at room temperature. Thereafter sections were washed three times in DPBS and blocked with 10% rabbit serum in DPBS for 45 min, to block residual unbound epitopes of the secondary anti-rabbit antibodies. Sections were then incubated with fluorophore labeled primary antibodies for 16-18 h at 4°C, washed thrice in DPBS, incubated with DAPI (cat#: 62248, ThermoFisher Scientific), at a dilution of 1:1000 for 5 minutes, washed again 3 times in DPBS and 2 times in ddH_2O and finally mounted in Aqua Polymount medium (cat#: 18606, Polysciences, Warrington, PA, USA). For immunofluorescence assays using antibodies from different host species, all primary antibodies were applied concomitantly for 16-18h at 4°C, sections were rinsed thrice in DPBS, incubated with appropriate secondary antibodies for 1h at room temperature, washed, DAPI counterstained and mounted as described above. 2% BSA and 5% fish gelatin in DPBS was used as antibody diluent in all assays. All antibodies and labelling kits used are summarized in Suppl.tab.1 and antibody combinations, dilutions and corresponding HIER treatments, for all IF stainings are detailed in Suppl.tab.2.

Microscopy and Quantification

Sections were imaged at an OLYMPUS BX63 fluorescence microscope, with motorized stage, using Olympus cellSens software (Olympus, Shinjuku, Tokyo, Japan). Tissue sections were scanned at 20x magnification using cellSens´ manual panoramic imagining (MIA) function, with automatic shading correction, at default settings. All downstream analyses were performed in QuPath [8]. Cell counts were obtained in perilesional cortical grey matter and white matter regions of the ipsilateral stroke lesioned hemisphere, as well as anatomically corresponding regions in the contralateral hemisphere and matched section from Sham operated animals. T2 weighted MRI images from the same animals were used to guide the definition of perilesional areas. Grey matter ROIs were defined as 1 mm^2 (800x1250µm) rectangles, at the border of the stroke lesion. Due to the variable area and contribution of large white matter tracts to the perilesional area, white matter ROIs of approximately 1 mm^2 were defined using QuPaths brush annotation tool, encompassing the corpus callosum and variable portions of the external capsule. Cells were identified using the Cell detection function, based on nuclear DAPI signal and intensity features, including Haralick features, as well as smoothed features (Radius(FWHM)=50 µm) were

computed for each channel of interest on every analysed tissue section. For standardized annotation of immunopositive cells, object classifiers were trained, using QuPaths´ random trees algorithm on at least 100 cells per tissue section, for each channel. The obtained cell counts were exported and normalized to 1 mm^2, for statistical analyses.

Purification of rodent oligodendrocyte precursor cells OPC

Primary rodent OPCs were purified using differential detachment as previously described [15], with minor modifications. Briefly, forebrains from a total of 12 E20 fetal rat cortices, derived from two timed pregnant Sprague Dawley rat dams (Charles river) were separated from meninges, dissected in ice cold HBSS (cat#: 14175095, Gibco, ThermoFisher Scientific) and enzymatically dissociated using Miltenyis Neural Tissue Dissociation Kit (P) (cat#: 130-092-628, Miltenyi) and a gentleMACS™ Octo Dissociator with Heaters (cat#: 130-096-427, Miltenyi) (program: 37C_NTDK_1), as per manufacturer's instructions. Ice cold DMEM/F12 + Glutamax 4 mM (cat#: 31331093, Gibco, ThermoFisher Scientific), supplemented with 10% heat inactivated fetal bovine serum (FBS) (cat#: 10500064, Gibco, ThermoFisher Scientific) was used to stop enzymatic dissociation and the cell suspension was filtered (70 µm filters) and centrifuged for 4 min at 300 g, at room temperature, on a swing bucket centrifuge. After decanting the supernatant, the cell pellet was suspended in mixed neural culture medium: DMEM/F12+ Glutamax 4 mM, 10% FBS, 1% Penicillin-Streptomycin (P/S) (cat#: 15140122, Gibco, ThermoFisher Scientific), 1% B27 supplement (cat#: 17504044, Gibco, ThermoFisher Scientific). Cells were seeded in Poly-L-lysin–hydrobromid (PLL) (cat#: P1524, Sigma Aldrich) coated T75 flasks (cat#: CLS430641U, Corning) at a density of approximately 3.5 x 10^6 cells per T75 flask and maintained in mixed neural culture medium for 8-10 days, with media half changes every 48 h. At day in vitro (DIV) 8-10 flasks were sealed air tight and shaken at 275 rpm, 37°C on an orbital shaker (MTS 4, IKA-Werke GmbH & Co. KG, Staufen, Germany) in a humidified incubator for 1h. This step detached the majority of loosely attached microglia, which were removed by a full media change with mixed neural culture medium. Thereafter, the T-75 flasks were allowed to equilibrate in a humidified incubator at 95%O_2/5%CO_2 for 2h, resealed and shaken at 300 rpm, 37°C for 16-18h. Supernatant with detached OPCs was collected, filtered (40µm filters) and plated in 94/1mm non-cell culture treated petri dishes (cat#: 632181, Greiner bio-one) and

incubated for 50 min in a humidified cell culture incubator. Supernatant with non-attached OPCs was collected, plates with attached residual microglia were discarded. OPCs containing supernatant was centrifuged at 300 g for 4 min and OPCs were resuspended in defined serum free OPC base medium. OPC base medium consisted of DMEM/F12 + Glutamax 4 mM, 1 mM sodium pyruvate (cat#: 11360070, Gibco, ThermoFisher Scientific), 10 ng/ml d-Biotin (cat#: B4639), 5 µg/ml N-Acetyl-L-cysteine (cat#: A9165), 62.5 ng/ml progesterone (cat#: P8783), 5 µg/ml Insulin (cat#: I6634), 40 ng/ml sodium selenite (cat#: S5261), 100 µg/ml Transferrin (cat#: T1147), 100 µg/ml BSA, all from Sigma Aldrich, 16 µg/ml putrescine (cat#: A18312, ThermoFisher Scientific), 1% P/S and 2% B27.

In vitro OPC migration assay

2 well culture-inserts (cat#: 80209, Ibidi, Gräfelfing, Germany), in PLL coated 4 well chamber slides (cat#: 354114, Falcon, Corning) were used for migration assays. 50 µl OPC cell suspension at a concentration of $1x10^6$ cells/ml were seeded in OPC base medium, supplemented with 20 ng/ml platelet-derived growth factor A (PDGF-A) (cat#: PPT-100-13A-50, Biozol, Eching, Germany), in each well. Cells were allowed to attach for 16-18 h. Thereafter, the culture-insert was removed leaving a defined 500 µm cell free gap. Medium was then changed to 500 µl OPC base medium (untreated control (=UC)) or OPC base medium supplemented with 1 ug/ml Osteopontin (cat#: 6359-OP, R&D Systems, Minneapolis, MN, USA) (OPN). After 48 h of migration cells were fixed with 4% paraformaldehyde in DPBS for 20 min at room temperature and washed three times with DPBS, followed by blocking and permeabilization in 2% BSA, 10% fish gelatin and 0.2% Triton-X. Cy3® conjugated anti-NG2, diluted 1:50 (cat#: AB5320C3, Sigma Aldrich) and CoraLite® Plus 488 conjugated Ki67, at a concentration of 2 µg/ml (cat#: Ab15589, Abcam, labelled with the FlexAble CoraLite® Plus 488 Antibody Labeling Kit Cat#: KFA001, Proteintech) were used to visualize OPCs and mitosis committed nuclei, respectively. 2% BSA and 5% fish gelatine in DPBS was used as antibody diluent and antibody dilutions were applied over night at 4°C. Thereafter cells were washed three times in DPBS, incubated with DAPI (1:1000) for 5 minutes, washed an additional three times in DPBS, and two times in ddH_2O before mounting in Aqua Polymount medium. All NG2 positive and NG2/Ki67 double positive cells within the 500 µm gap area, of each replicate, were counted at a OLYMPUS BX63

fluorescence microscope using Olympus cellSens software (Olympus, Shinjuku, Tokyo, Japan).

Bromodeoxyuridine (BrdU) incorporation assay

BrdU incorporation assays were used to assess OPC proliferation *in vitro*. OPCs were plated on PLL coated cover slips (cat#: CB00120RA020MNZ0, Epredia, Portsmouth NH, USA), in 24 well plates (cat#: 3527, Costar, Corning) at a density of $0.5x10^5$ cells per well in OPC base medium, supplemented with 20 ng/ml PDGF-A and were allowed to attach and equilibrate for 24h. Thereafter, PDGF-A supplemented medium was removed and cells were rinsed once in OPC base medium to remove residual PDGF-A. OPCs were then treated with osteopontin at a concentration of 1 µg/ml (OPN condition) untreated OPCs in OPC base medium alone served as controls (UC condition). Cells were treated for 24 h, during the last 6 h 10 µM BrdU (cat# 51-2420KC) was added. Cells were fixed and permeabilized with BD Cytofix/Cytoperm buffer (cat# 51-2090KE) for 20 min, washed thrice in BD Perm/Wash buffer (cat# 51-2091KE) and refixed for an additional 10 min in BD Cytofix/Cytoperm buffer, followed by incubation with 300 µg/ml DNAse (cat# 51-2358KC) in DPBS at 37°C for 1 h to expose nuclear BrdU, as per manufacturers recommendations. All reagents from BD Bioscience (Franklin Lakes, NJ, USA).

Cells were then washed thrice in BD Perm/Wash buffer, blocked with 2% BSA, 10% fish gelatine in DPBS for 30 min and FITC conjugated anti-BrdU antibody (cat# 51-2356KC, BD Bioscience), and Cy3® conjugated anti-NG2 (cat# AB5320C3, Sigma Aldrich), both diluted 1:50 in 2% BSA and 5% fish gelatine in DPBS were applied. After overnight incubation, cells were washed thrice in DPBS, incubated with DAPI (1:1000) for 5 minutes, washed an additional 3 times in DPBS, and 2 times in ddH2O before mounting in Aqua Polymount medium. For each condition 4 cover slips were imaged and NG2 positive and NG2/BrdU double positive cells in 2 random 20X magnification fields of view per cover slip were counted at an OLYMPUS BX63 fluorescence microscope using Olympus cellSens software.

Statistical analyses

For cell counts from IF stainings´ in tissue sections we performed Kruskal-Wallis-H-Tests, followed by Dunn's post hoc comparisons, as the data structure did not satisfy the prerequisites for parametric tests. Cell counts obtained from cell culture assays

were analysed using unpaired Student´s t-tests. Cell counts are reported as mean ± SD through the main text and represented as box plots, depicting medians, 25th to 75th percentiles as hinges, minimal and maximal values as whiskers, and individual counts as dots throughout all respective figures. A p-value of <0.05 was set as threshold for statistical significance. All statistical analyses were carried out using GraphPad Prism v.9.0.0 (GraphPad Software).

Results

MCAO alters CNS cell type composition and induced cell type specific transcriptional changes

Here we used a rodent model of permanent middle cerebral artery occlusion (MCAO) to investigate acute cell type specific transcriptional perturbations, at single cell resolution in the acute phase following cerebral ischemic injury (Fig.1a).

The induction of ischemic brain tissue damage was validated by MRI imaging 48 h after injury (Suppl.Fig.1). Hyper intense lesions were absent from all Sham operated rats (n=4), while animals from the MCAO group (n=7) exhibited pronounced ischemic lesions ranging from 35.01 to 617.2 mm^3, which we further stratified into moderate MCAO (mMCAO) (59.6±39.2, n=3) and severe MCAO (sMCAO) (449.5±132.5, n=4) infarctions (Fig.1a, Suppl.Fig.1). Selection of coronal tissue sections for snRNAseq was guided by MRI imaging data. The maximum extent of the ischemic brain lesions was localized approximately between Bregma anterior-posterior +1.5 mm and -2 mm, in all MCAO samples, thus this region was selected for snRNAseq (Suppl.Fig.1). Left and right hemispheres were sequenced separately. Hence, we obtained datasets from the left and right hemispheres of Sham operated rats (Sham L and Sham R, respectively), as well as left (=contralateral to ischemic lesion) and right (= ipsilateral to ischemic lesions) hemispheres of mMCAO and sMCAO infarcted rats (mMCAO contra, mMCAO ipsi, sMCAO contra, sMCAO ipsi, respectively) (Fig.1a).

After quality control, filtering and integration we recovered a total of 68616 high quality nuclear transcriptomes (between 8123 and 13461 per dataset, Suppl.data.file.2), with a median of 2585 UMIs and 1347 genes per nucleus. Major quality control metrics for all individual datasets are reported in Suppl.Fig.2a. Following unbiased clustering

analysis, we first grouped all nuclei into 6 non-neuronal and 23 neuronal (12 glutamatergic, 1 cholinergic, 10 GABAergic) major cell clusters (Fig.1b), using well established marker genes (Fig.1c). We identified three neuroglia clusters, specifically one immature and one myelinating/mature oligodendrocyte lineage cluster (OLIGO_1 and OLIGO_2, respectively) and one astrocyte clusters (AC), as well as one ependymal and mural cell cluster (EP_M_C), one vascular cell cluster, enriched for endothelial and pericyte transcripts (VASC) and one myeloid cell cluster (MC). Glutamatergic neurons were broadly split into *Satb2* expressing (GLU_Satb2+), thus predominantly isocortical and *Satb2* negative, thus predominantly allocortical, and deep grey matter glutamatergic neurons (GLU_Satb2-). As previously described GLU_Satb2+ neurons could be well segregated using cortical layer specific markers. We identified one cholinergic interneuron cluster (CHOL_IN). GABAergic neurons grouped into various interneuron (GABA_IN) and medium spiny neuron populations (GABA_MSN). GABA_IN were moreover separated into various *Adarb2* positive (GABA_IN_Adarb2+), thus likely caudal ganglionic eminence (CGE) derived and *Adarb2* negative (GABA_IN_Adarb2-), thus likely medial ganglionic eminence (MGE) derived inhibitory interneuron clusters. One GABAergic cluster could not be characterized using known inhibitory subset specific markers and was thus termed ambiguous GABAergic neuronal cluster (GABA_Amb). A detailed description of this and all following sub clustering analyses, including the curation of marker genes is given in the supplementary notes.

Most of the clusters were represented in all datasets (Fig.1d, Suppl.Fig.2b). As expected, neuronal clusters were depleted in the dataset derived from sMCAO ipsi (Fig.1d, Suppl.Fig2b). Most strikingly, almost all captured MC transcriptomes were derived from the MCAO ipsi datasets. Their transcriptional signature significantly overlapped with the recently established gene expression profile of stroke-associated myeloid cells (SAMC) [10] (Fig.1e, Suppl.Fig.3.a) and they expressed both canonical microglia and macrophage, but not lymphocyte markers (Suppl.Fig.3b). Sub clustering analyses of the MC cluster revealed two microglia (MG_0, MG_1), three macrophage transcript enriched (MΦe_1 to 3) and one dendritic cell (DC) cluster (Suppl.Fig.3c,d). Notably, the expression of SAMC signature genes was well conserved across MG_1 and MΦe_1 to 3 (Suppl.Fig.3d), suggesting that microglia and macrophages converge onto a common phenotype within infarcted brain parenchyma, as previously reported [10]. We then systematically assessed overlaps between the gene signatures of the

stroke enriched myeloid cells in our datasets and previously described microglia and macrophage gene expression profiles in normal development and various neuropathologies. MG_1 and MΦe_1 to 3 exhibited robust enrichment for Axon Tract-Associated Microglia (ATM) [38] and disease-associated microglia (DAM) but not disease inflammatory macrophage (DIM) [89] associated transcripts (Suppl.Fig.3d,e). Furthermore, these clusters overlapped clearly with the transcriptional phenotype of "foamy" microglia enriched in multiple sclerosis (MS) chronic active lesion edges [1], while the profile of iron associated, activated MS microglia [1, 84] was more restricted to MΦe clusters and less prominently represented in our dataset. Likewise, the upregulation of protein synthesis associated genes (e.g. *Rpl13*, *Rplp1*) typical for iron metabolism associated and activated MS microglia [1, 84], was largely restricted to MΦe clusters. Other MS associated myeloid cell profiles (for example associated to chronic lesions, antigen presentation and phagocytosis) mapped more diffusely over all myeloid cell clusters (Suppl.Fig.3e). Lastly, microglia but not macrophage enriched clusters expressed proliferation associated genes (e.g. *Cdc45, Mki67, Top2a*) (Suppl.Fig.3d,e). Congruently, GO terms derived from microglia sub cluster markers where dominated by mitosis associated processes (Suppl.Fig.3f). Enrichment analysis of MΦe cluster markers highlighted various degranulation, endo-/phagocytosis, as well as iron and lipid transport and metabolism related processes (Suppl.Fig. 3f). MΦe cluster markers also indicated the production of and reaction to reactive oxygen (ROS) and nitrogen species (RNS) (Suppl.Fig.3f). Notably, some of the genes involved in these processes (e.g. *Dab2*, *Lrp1*, *Ctsd*) were also partially enriched in MG_1 (Suppl.Fig.3f). Taken together these findings underpin the emergence of the SAMC phenotype in the infarcted brain parenchyma and additionally highlight shared and distinct transcriptional signatures of stroke associated myeloid cell subsets.

We next investigated transcriptional perturbations induced by cerebral ischemia within those major cell clusters, which were represented in all datasets. We first compared the gene expression signatures of the left and right hemisphere derived from Sham control animals. As we did not identify any major differences in gene expression between the two Sham hemisphere datasets (Suppl.Fig.4a,b), they were pooled in all subsequent analysis. We next separately compared the datasets derived from moderately and severely infarcted hemispheres (mMCAO and sMCAO ispi, respectively) to the pooled Sham dataset. Both comparisons yielded a similar DEG distribution, with astrocyte and oligodendrocyte lineage cells emerging as the most

reactive populations (Suppl.Fig.4c,d). To increase the statistical power and hence robustness of our analysis we next pooled the mMCAO and sMCAO datasets and performed cluster-wise comparisons against the pooled Sham and MCAO contra datasets. Congruently, the majority of DEGs was derived from neuroglia clusters in both DEG calculations (Fig.1f, Suppl.Fig.4e,f). With the exception of OLIGO_1 and OLIGO_2, the gene expression profiles of clusters from the MCAO contra group and their Sham counterparts were mostly similar (Suppl.Fig.4g). The comparisons of the MCAO ipsi datasets to either Sham or MCAO contra datasets consistently unveiled a higher number of DEGs in excitatory neuronal clusters, as compared to inhibitory neuronal clusters (Fig.1f, Suppl.Fig.4.c-f, Suppl.Fig.5a,b). However, within the MCAO ipsi dataset we noticed the emergence of a canonical cellular stress response signature [31], marked by the upregulation of several heat shock proteins (e.g. *Dnaja1, Hsp90aa1, Hspa8, Hsph1*) in GABA_Amb (Suppl.Fig.5b). This signature mapped to a discrete subset of this cluster, which upon unsupervised subclustering analysis was revealed to be carried exclusively by misclustered oligodendrocytes but not neurons (Suppl.Fig.5c,d). Hence, this cluster did not disclose a set of neurons with particular vulnerability to ischemia, but rather underpinned the responsiveness of neuroglia to ischemic injury. A full list of DEGs per cell cluster across all mentioned comparisons is provided in Suppl.data.file.3.

Single nucleus transcriptomics identifies stroke specific oligodendrocyte lineage cell populations

Neuroglia are known drivers of regenerative mechanisms following stroke [43, 101], consist of highly heterogeneous subpopulations and ranged among the most transcriptional perturbed cell populations within our dataset. Therefore, we interrogated these cell populations in more detail. We first jointly sub clustered OLIGO_1 and OLIGO_2. After manual removal of two clusters with evident neuronal transcript contamination (Suppl.Fig.6a-d), 10 sub clusters remained, which could be largely grouped according to canonical developmental stages of the oligodendrocyte lineage trajectory. Specifically, we identified two oligodendrocyte precursor cell clusters (OPC_0, OPC_1), one committed oligodendrocyte precursor cell cluster (COP), one newly formed oligodendrocyte cluster (NFOLIGO), two myelin forming oligodendrocyte clusters (MFOLIGO_1 and MFOLIGO_2) and three mature oligodendrocyte clusters (MOLIGO_1 to MOLIGO_3) (Fig.2a). Lastly, one sub cluster faintly expressed markers

637 of oligodendrocytes and immune cell associated genes (Fig.2a). Strikingly, the majority
638 of immune cell transcripts, within this sub cluster was derived from the MCAO ipsi
639 datasets (Suppl.Fig.6e, Supplementary notes). Importantly, previous research has
640 shown that oligodendrocyte transcripts accumulate in the nuclear compartment of
641 phagocytic myeloid cells, giving rise to clusters expressing both oligodendrocyte and
642 myeloid cell transcripts *in vivo* [84]. This cluster was thus annotated myeloid cell
643 oligodendrocyte mixed cluster (MC_OLIGO). Details on marker gene curation are
644 given in the supplementary notes, a full list of subcluster markers is provided in
645 Suppl.data.file.2.

646 Notably, the two subclusters, OPC_1 and MOLIGO_1, were predominantly derived
647 from infarcted brain tissue of sMCAO and to a lesser extent from mMCAO (Fig.2a,
648 Suppl.Fig.6f,g). Pseudotime trajectory analysis indicated that the stroke specific sub
649 cluster OPC_1 branched directly from the conserved sub cluster OPC_0 (Fig.2b). As
650 expected, the mature oligodendrocyte clusters were associated to the highest pseudo
651 time values. We identified a prominent trajectory bifurcation within MOLIGO_0, with
652 one stroke specific branch encompassing MOLIGO_1 and one branch extending to
653 MOLIGO_2, which was conserved across all groups. Notably, cell cycle scoring
654 revealed that sub cluster OPC_1 was derived from proliferating cells (Fig.2b).

655 We next conducted DEG calculations for the oligodendrocyte lineage subclusters
656 which were conserved across all groups. (Suppl.Fig.7). Remarkably, the gene
657 expression profiles of the conserved clusters differed little between the infarcted and
658 contralateral hemisphere, with the exception of MC_OLIGO (Suppl.Fig.7a), which was
659 enriched in immune process and myeloid cell associated genes in MCAO ipsi as
660 described above (Suppl.Fig.6e). Likewise, the gene expression profiles of most
661 conserved clusters were similar in the MCAO ipsi and Sham datasets, with the notable
662 exception of OPC_0 (Total DEG: 50), MOLIGO_0 (Total DEG: 185) and MC_OLIGO
663 (Total DEG: 98) (Suppl.Fig.7b). Interestingly, MOLIGO_0 emerged as the only cluster
664 with notable transcriptional perturbation from the comparison of the MCAO contra to
665 the Sham datasets (Total DEG: 119) (Suppl.Fig.7c). Importantly, 102 [96,23%] of the
666 downregulated DEGs in the MOLIGO_0 subcluster in MCAO contra relative to Sham,
667 were also identified in the comparison of MCAO ipsi to Sham (Suppl.Fig.7d) and
668 contained neurexins and neuregulins (e.g. *Nrxn1*, *Nrxn3*, *Nrg1*, *Nrg3*), as well as genes
669 encoding neurotransmitter receptors, ion channels and ion channel interacting proteins

(e.g. *Kcnip4*, *Grm5*, *Kcnq5*) (Suppl.Fig.7e). Of note, the downregulation of many of these genes was subtle in terms of gene expression, as they were a priori expressed at low levels in the Sham dataset within the oligodendrocyte lineage clusters (Suppl.Fig.7e). All DEGs, derived from all mentioned comparisons are reported in Suppl.data.file.4.

We next interrogated how the MCAO ipsi specific sub clusters (OPC_1 and MOLIGO_1) differed transcriptionally from their homeostatic counterparts, via DEG analyses. Comparisons of OPC_1 to OPC_0 and MOLIGO_1 to MOLIGO_2 yielded a total of 519 and 384 DEGs, respectively (Fig.2c, Suppl.data.file.4). Notably, the OPC_1 and MOLIGO_1 DEG signature was identified in both mMCAO ipsi and sMCAO ipsi datasets (Suppl.Fig.6h,i). To gain insight into how the stroke specific OPC_1 and MOLIGO_1 gene expression signatures might relate to changes in biological function we performed enrichment analyses (summarized in Suppl.data.file.5). We also systematically compared the signatures of OPC_1 and MOLIGO_1 to each other and to gene expression profiles of diseases associated oligodendrocytes (DAO), derived from various rodent models of neurodegeneration and demyelination [73] (Suppl.Fig.8, Supp.data.file.1). Transcriptional overlaps between stroke specific oligodendrocyte lineage sub clusters with DAO profiles were generally limited (Suppl.Fig.8). The vast majority of OPC_1 enriched genes mapped to cell cycle progression and proliferation associated terms (Fig.2d, Suppl.data.file.5). Enrichment analyses further highlighted, the upregulation of several intracellular scaffold proteins and protein-kinases involved in OPC cell adhesion, migration, survival and differentiation, such as *Iqgap1* [71], *Met* [4]*, Fyn* [54]*,* or *Axl* [85] and indicated extensive interactions of OPC_1 with the extracellular matrix (ECM) (Fig.2d). Notably, the canonical pan-reactive astrocyte markers *Cd44* and *Vim* [59, 103], as well as *Runx1* were enriched in both DAO and OPC_1. *Runx2* was likewise upregulated in OPC_1, as well as the neuroprotective immunomodulatory alarmin *Il33 [100].* Interestingly, both *Vim* and *Il33,* have previously been shown to be upregulated upon injury in various oligodendrocyte lineage cells [32, 50]. Notably, several growth factors, such as *Ccnf, Vgf* and *Fgf2* were also upregulated in OPC_1. Conversely, we observed a downregulation of synaptic transmission associated transcripts, particularly concerning potassium and glutamate homeostasis in OPC_1 (Fig.2d).

Interestingly, multiple biological processes associated to MOLIGO_1 enriched DEGs, for example Axonogenesis (GO:0007409), or Axon Guidance (R-HSA-422475) (Suppl.data.file.5), relate to the modulation of neuritogenesis. Several genes encompassed by these gene sets, such as multiple upregulated sempahorines, have more extensive pleiotropic roles in physiological CNS development and pathology [19]. Similar to OPC_1 several MOLIGO_1 enriched DEGs were associated to ECM interactions and glycosaminoglycan (GAG) metabolism (Fig.2d). Many of the MOLIGO_1 enriched DEGs (e.g. *Dlg1*, *Lamc1*, *Psem4*, *Sema5b*, or *Cadm1*) were also expressed in less mature oligodendrocyte sub clusters, but absent in the mature oligodendrocyte populations MOLIGO_0 and MOLIGO_2, in the Sham and MCAO contra datasets. Congruently, the expression of the canonical COP and NFOLIGO marker *Bcas1* [29] was markedly higher in MOLIGO_1 as compared to MOLIGO_0 and MOLIGO_2. Thus, several markers of more immature oligodendrocyte developmental stages were uniquely upregulated in MOLIGO_1, but not other mature oligodendrocyte clusters. Several MOLIGO_1 enriched DEGs were related to Notch, TGF-β and IGF-1 signalling, but also included more elusive signalling molecules, like the TIR-domain-containing adaptor (TRIF) recruiter *Wdfy1* [41] (Fig. 2d). Notably, several of the genes associated to Notch signalling by enrichment analyses, such as *Il6st* and *Stat3* are also crucially involved in multiple type I cytokine signalling pathways [69].

Regarding putative metabolic changes, we noted a robust upregulation of the 6-phosphofructo-2-kinase/fructose-2,6-biphosphatase isozyme 3 and 4 coding genes *Pfkb3*, *Pfkb4*, signifying a state of increased anaerobic glycolysis [61]. This was accompanied by a downregulation of aspartate/asparagine metabolism related transporters (e.g. *Slc25a13*) and enzymes (e.g. *Folh1, Aspa*) and P-Type ATPases involved in lipid translocation (*Atp10a,11a,11b*). Moreover, myelination associated genes were discreetly downregulated in MCAO ipsi derived MOLIGO_1 transcriptomes as compared to MOLIGO_2 (Fig.2c,d).

Complementary to the calculation of DEGs between a priori defined clusters, we identified genes which changed dynamically as a function of pseudo time and combined them into co-regulated gene modules using Monocle 3 (see Materials and Methods) (Fig.2e). Remarkably, 5 modules mapped uniquely to stroke specific sub clusters and mainly consisted of genes which were also identified as OPC_1 or

MOLIGO_1 enriched DEGs (Fig.2e, Suppl.data.file.6). Interestingly, the OPC_1 associated modules 4 and 11 consisted mainly of proliferation related genes and mapped over the entire OPC_1 cluster. By contrast, module 5, which contained ECM-interaction, migration, survival and immunomodulatory process associated genes appeared further down on the pseudo temporal trajectory. The aggregate rank score of module 9 increased with incremental distance to the trajectory bifurcation within MOLIGO_0, indicating a dynamic progression from MOLIGO_0 towards MOLIGO_2 specifically within infarcted tissue. This module was permeated by abundant ECM and cell-cell interaction associated genes (e.g. *Adamts1, Cadm1*, *Cldn14*, *Col12a1*), as well as other genes previously identified as MOLIGO_1 markers during DEG analysis, as described above (e.g. *Stat3*, *Wdfy1*).

Additionally, we inferred transcription factor (TF) activities using a molecular foot print based approach [6]. In congruence with the previous analyses several TFs for which increased activation was inferred within OPC_1 pertained to proliferation and survival associated pathways, for example E2f1, or Myc [64] (Fig.2f). Notable, TFs with increased activity in MOLIGO_1 included the hypoxia response related basic helix–loop–helix/Per-ARNT-SIM (bHLH–PAS) superfamily members Ahr and Hif1α [53] and the STAT family members Stat3 and Stat5a. Conversely, the inferred activity of multiple hallmark TFs of oligodendrocyte differentiation and myelination, such as Olig1 [24], Nkx2-2 [77], or Rxrg [42] was decreased in the MCAO ipsi derived MOLIGO_1 nuclei (Fig.2f). In summary, using multiple complementary bioinformatics approaches we described the emergence of two transcriptionally unique oligodendrocyte lineage clusters within the infarcted hemisphere, marking the most robust cerebral ischemia induced change within the oligodendrocyte lineage.

Proliferating, VIM and IL33 positive OPCs accumulate at the perilesional zone

We next conducted IF staining to confirm the presence of stroke associated proliferating OPCs *in vivo* and interrogated their spatial distribution in the MCAO infarcted brain, 48h after stroke (Fig.3). Overall, mitosis committed OPCs ($NG2^+/Ki67^+$) were almost absent in cortical grey matter (GM) and large white matter (WM) tracts of Sham operated animals, sparse in the hemisphere contralateral to the infarct lesion, but abundant in the perilesional grey and white matter surrounding the ischemic lesion (Fig.3). Furthermore, a substantial number of mitotic OPCs was also positive for VIM and IL33 (Fig.3), as predicted by snRNAseq analysis (Fig.2).

Specifically, while essentially absent in the GM and WM of Sham operated rats (GM: 0/mm^2; WM: 1.05±1.2/mm^2) and the hemisphere contralateral to infarction (GM: 0.3±0.5/mm^2; WM: 0.9±1.1/mm^2) the number of NG2$^+$/VIM$^+$/Ki67$^+$ triple positive OPCs increased significantly in the perilesional GM (53.9±18.3/mm^2) and WM (18.6±5.1/mm^2) (Fig.3a-c).

Likewise, virtually no NG2$^+$/IL33$^+$/Ki67$^+$ triple positive OPCs were found in the grey and white matter of Sham operated and contralateral MCAO brains (Fig.3d-f). In contrast, the number of NG2$^+$/IL33$^+$/Ki67$^+$ triple positive OPCs in the perilesional GM increased significantly as compared to corresponding Sham GM (35.7±26.3/mm^2) (Fig.3f). Similarly, no NG2$^+$/IL33$^+$/Ki67$^+$ triple positive OPCs were identified in the WM of Sham operated animals, or the WM contralateral to infarction, while they were abundant in perilesional WM (17.00±5.5/mm^2) (Fig.3d-f). Statistical comparison of all subsets within all ROIs is reported in Suppl.data.file.7.

Collectively, these findings confirmed that mitotic OPCs distinctly accumulate in both the perilesional WM and GM, 48h after MCAO and a substantial subset of these OPCs expresses the snRNAseq predicted, injury associated markers VIM and IL33.

Transcriptional heterogeneity of reactive astrocytes in the infarcted brain

Similar to our investigation into the heterogeneous responses to stroke in oligodendrocyte lineage subsets we performed subclustering analysis for astrocytes. After removal of contaminating clusters (Suppl.Fig.9), we identified 5 astrocyte sub clusters. 2 sub clusters (AC_1 and AC_2) exhibited robust expression of homeostatic astrocyte associated genes such as *Gpc5*, *Kirrel3*, *Cdh10* or *Trpm3* [1, 36, 84]. These clusters were identified in all datasets, although their relative abundance decreased slightly in the contralateral hemisphere of MCAO operated rats and substantially in the ipsilateral, infarcted hemisphere (Fig.4a). Conversely, in three subclusters (AC_3 to AC_5) these homeostatic astrocyte markers were expressed more faintly, while they were enriched for pan reactive astrocyte markers such as *Gfap*, *Vim*, *Osmr*, *Cd44*, or *Cp [59, 103]* (Fig.4a). These three clusters were virtually absent from Sham datasets, sparsely represented in datasets of the contralateral MCAO hemisphere, abundant in infarcted hemispheres (Fig.4a, Suppl.Fig.9e) and thus were annotated as reactive astrocyte clusters. Further details on marker gene curation are given in the supplementary notes. Of note reactive astrocytes were more abundant in the datasets derived from severe, compared to moderate infarctions (Suppl.Fig9f). To characterize

these reactive astrocyte populations in more detail, we compared each reactive astrocyte cluster to the homeostatic subclusters (AC_1 and AC_2) using DEG analyses (Fig.4b, Suppl.data.file.8). Notably, the DEG signature of AC_3 was prominent in both moderate and severe infarctions, while the AC_4 and AC_5 reactive astrocyte signature was predominately derived from severe infarctions (Suppl.Fig.9g-i). Inference of functional characteristics from the DEGs of the reactive astrocyte subclusters (AC_3 to AC_5), using enrichment analyses highlighted notable communalities, particularly between the gene signatures of AC_3 and AC_4 (Fig. 4c, Suppl.data.file.9). For instance, tight (e.g. *Tjp1*, *Tjp2*) and adherence (e.g. *Vcl*) junction components related to blood brain barrier maintenance were upregulated in both AC_3 and AC_4. Furthermore, several upregulated DEGs in AC_3 and AC_4 related to various ECM interaction, wound healing and cell motility and migration related terms to varying degrees. For example, some cadherin binding related genes (e.g. *Cald1*, *Cdh2*) were more enriched in AC_3, matrix metalloprotease coding genes (e.g. *Adamts1*, *Adamts9*) were upregulated in both, as was *Cd44*, and various Integrin family member (e.g. *Itga1, Itga5*). Various reactive astrocyte derived DEGs related to axon guidance and neural cell migration, such as *Sema3c* [81] in AC_3 or *Robo2* [47] in AC_4. Other related to VEGF response (e.g. *Nrp2*, *Rock2*, *Hspb1*) predominantly in AC_4 and chemokine signalling (e.g. *Ccl2*, *Shc3*, *Shc4*) predominately in AC_3. Overall the transcriptional signature of AC_3 and AC_4 suggest a complex injury response, marked by ECM reorganization, increased migration and involvement in bidirectional communication with other brain parenchymal and infiltrating cell types. AC_5 lacked several of the aforementioned transcriptional features of AC_3 and AC_4, but shared the upregulation of several pan reactive astrocyte markers such as *Gfap*, *Cp*, or *Vim* with the other reactive astrocytes (Fig.4a, Suppl.Fig10a). The most distinguishing characteristic of AC_5 was the enrichment of several gene sets related to cilium and axonemal assembly and movement, including the cilliogenic transcription factor *Rfx3*, cilium dynein arm (e.g.*Dnah9*), or central pair (e.g. *Cfap46, Cfap54*) elements [44] (Fig. 4d). Of note this profile was identified in the AC_5 cluster in MCAO ipsi and MCAO contra.

Multiple glutamate (e.g. *Grin2c, Gria2*) and GABA (e.g. *Gabrb1, Gabrg1*) receptors, glutamate (e.g. *Slc1a2*) and GABA (e.g. *Slc6a11*) reuptake transporters and other solute carrier (SLC) transporters, involved in amino acid import (e.g. *Slc7a10*) were robustly downregulated in all reactive astrocyte subclusters (Fig.4e). Several genes

related to lipid metabolism (e.g. *Acsl3*, *Acsl6*) and lipid transport (e.g. *Abca1, Apoe*) were particularly downregulated in AC_3. Genes involved in synapse assembly and maintenance, such as *Gpm6a* were downregulated in all reactive astrocyte subsets to various degrees. To summarize, reactive astrocytes lost homeostatic gene signatures related to neurotransmitter and lipid metabolism, as well as synapse maintenance in infarcted brain tissue.

The inference of TF activities unveiled further shared patterns in reactive astrocytes. Notable examples of TFs with increased activity in reactive astrocytes related to STAT signalling (e.g. Stat3, Stat5a/b), proliferation, growth and survival (e.g. E4f1, Myc, Jun, Fos, Fosl2), response to hypoxia (e.g. Hif1a) and growth factors (e.g. Egr1) [88], or Snai1, which was recently implicated in the TGF-beta induced glial-mesenchymal transition of Müller glia [46]. Notably, increased activity for multiple of these TFs (e.g. Stat5a, Stat3, Myc, Hif1a, Snai1) was also observed in stroke specific Oligodendrocyte subsets (Fig.2f). Congruent with the upregulation of primary cilium associated genes, increased activity of the cilliogenesis master regulator Foxj1 [44] was inferred for AC_5.

Next we compared the transcriptional signatures of the stroke associated reactive astrocytes within our dataset to gene expression profiles of reactive astrocytes found in other neurodegenerative and inflammatory neuropathologies (Suppl.Fig.10). Pan-reactive [59] and neurodegenerative disease associated astrocyte (DAA) [36] signatures, mapped to several stroke reactive astrocyte subsets (Suppl.Fig.10a,c-d). No stroke reactive astrocyte subset in our dataset matched the inflammatory, neurotoxic A1 phenotype, while the neuroprotection associated A2 signature [59, 103] partially overlapped with the signature of AC_3 (Suppl.Fig.10d). Among the reactive astrocyte populations identified in MS (MS_AC_reactive) by Absinta et al. [1], the MS_AC_reactive_1&5 subsets, originally described as “reactive/stressed astrocytes” partially overlapped with the stroke reactive astrocyte clusters AC_3 and AC_4 of our dataset (Suppl.Fig.10c,d). Overlaps with the “astrocytes inflamed in MS” (MS_AIMS) signature were sparse and mainly restricted to pan reactive astrocyte genes (e.g. *Vim*, *Gfap*) (Suppl.Fig.10c,d). Interestingly, 25 (19.38%) of the 129 DEGs upregulated in AC_5 were also included in MS_AC_reactive_4, originally described as “senescent astrocytes” [1] (Suppl.Fig.10c). However, these overlaps did not consist of genes related to senescence, but almost exclusively ciliary process associated genes. Remarkably, the gene expression profiles of reactive astrocytes and stroke specific

oligodendrocyte lineage subsets within our dataset shared extensive similarities (Suppl.Fig.10e). Particularly, we observed that 66 of the 351 DEGs (18.8%) upregulated in OPC_1 and 24 of the 216 DEGs (11.11%) upregulated in MOLIGO_1 were also upregulated in the reactive astrocyte cluster AC_3 (Suppl.Fig.10e).

Cell-cell communication (CCC) inference analysis implicates glycoproteins as major immuno-glial signalling hubs in infarcted brain tissue

So far we identified transcriptionally unique myeloid and neuroglial subsets within infarcted brain tissue. Therefore, we next interrogated the molecular cross talk between these cells by inferring potential ligand receptor (LR) interactions, using LIANA. We only retained the most robust interactions (aggregate rank score ≤0.05) (Suppl.data.file.10) and extracted LR pairs unique to datasets from MCAO ipsi. Intriguingly, we inferred 129 LR pairs specific to infarcted brain tissue and grouped them into immuno-glial (Suppl.Fig.11a-e) and intra-glial (Suppl.Fig.12a-e) interactions. These interactions corroborated multiple recently inferred stroke response signalling axes, for example between microglia and oligodendrocyte lineage subsets (e.g. Igf1->Igf1r, Thbs1->Cd47, Psap->Gpr37) [45]. Interestingly, within infarcted tissue specifically, macrophage enriched myeloid cell clusters (MΦe) were predicted to signal abundantly via Fibronectin (*Fn1*) onto both myeloid and neuroglia subsets (Suppl.Fig.11b-d). Cell surface glycoproteins, such as myelin associated glycoprotein (*Mag*), various integrin and syndecan family members and CD44 were the most commonly predicted Fibronectin receptors on myeloid and neuroglial cells (Suppl.Figs.11-12). Notably, astrocytes were also predicted to signal via fibronectin -> glycoprotein receptor signalling onto various myeloid and neuroglial subsets (Suppl.Figs.11e-12d,e). Glycoprotein receptors indeed emerged as signalling hubs on various myeloid and neuroglial subsets. For instance, Cd44 was inferred to be targeted by various ECM associated ligands such as fibronectin (*Fn1*), various collagens (e.g. *Col4a1*, *Col6a3*), *Spp1* encoding osteopontin, but also growth factors, such as hepatocyte growth factor (*Hgf*) or heparin-binding EGF-like growth factor (*Hbegf*) (Suppl.Figs.11-12). Strikingly, microglia and macrophage derived *Spp1* was predicted to signal back to both myeloid subsets, as well as stroke specific OPCs (OPC_1) and stroke reactive astrocytes (AC_3 and AC_4) via *Cd44* (Suppl.Figs.11b-d).

Cd44 positive reactive astrocytes and proliferating OPCs accumulate at the lesional rim in close proximity to osteopontin positive myeloid cells

CD44 was identified as a particularly robust marker of reactive astrocytes, in various neuropathological contexts [65] and our dataset (Fig.4, Suppl.Fig.10). Surprisingly, we also detected a pronounced upregulation of *Cd44* in stroke associated, proliferating OPCs (Fig.2). Moreover, *Spp1 -> Cd44* signalling events from myeloid cells to stroke specific OPCs, reactive astrocytes and myeloid cells themselves ranged among the most robustly predicted interactions within our CCC analysis (Suppl.Figs.11-12). We reasoned that these cell populations might distinctly spatially colocalize in the infarcted brain, a hypothesis we interrogated using IF stainings.

Indeed, the number of $GFAP^+/CD44^+/VIM^+$ reactive astrocyte was significantly higher in perilesional cortical GM (123.6 ± 107.9/mm^2) as compared to the contralateral GM in MCAO operated rats (4.2 ± 3.9/mm^2) and the GM of Sham operated rats (2.8 ± 3.3/mm^2) (Fig.5a-c). Likewise, $GFAP^+/CD44^+/VIM^-$ astrocytes were significantly more abundant in perilesional (41.4 ± 21.9/mm^2) as compared to contralateral MCAO group GM (4.2 ± 6.1/mm^2). Comparison of cell numbers in perilesional to Sham (5.3 ± 3.3/mm^2) GM approached significance (Fig.5c). CD44 was previously implicated as a WM astrocyte subset marker [84]. Congruently, $GFAP^+/CD44^+/VIM^-$ astrocytes were found in all imaged WM ROIs (Sham: 120.3±64.9/mm^2; MCAO contra: 116.9±101.8/mm^2; MCAO ipsi: 301.4± 485.7/mm^2) and did not differ significantly between groups. However, the abundance of $GFAP^+/CD44^+/VIM^+$ astrocytes in the perilesional WM (626.0±306.8/mm^2) increased significantly as compared to MCAO contra (88.4±35.9/mm^2) and comparison to Sham WM (120.0±44.04/mm^2) approached significance (Fig.5c).

Proliferating CD44 positive OPCs ($NG2^+/CD44^+/Ki67^+$) were essentially absent from the GM or WM of Sham treated rats (GM: 0, WM: 0.25±0.5/mm^2) or the hemisphere contralateral to infarction (GM: 0, WM:0), while they were significantly more abundant in perilesional GM (44.3±23.7/mm^2) and WM (12.3±10.2/mm^2) (Fig. 5d-f).

In summary, both reactive astrocytes ($GFAP^+/CD44^+/VIM^+$) and proliferating CD44 positive OPCs ($NG2^+/CD44^+/Ki67^+$) accumulated in the perilesional zone surrounding the infarcted tissue.

Within the same region we identified abundant OPN positive myeloid cells (Iba1$^+$/OPN$^+$) (Fig.6a-c). Specifically, the number of Iba1$^+$/OPN$^+$ cells within the perilesional GM (161.3±44.4/mm^2) was significantly higher as compared to the GM contralateral to infarction (11.6±9.4/mm^2) or the GM of Sham operated rats (17.3±18.4/mm^2) (Fig.6c). Likewise, significantly more Iba1$^+$/OPN$^+$ cells were identified in the perilesional WM (226.3±135.3/mm^2) as compared to the WM contralateral to infarction (11.385±18.25/mm^2) and the comparison to Sham WM (11.6±9.5/mm^2) approached statistical significance (Fig.6c). Notably, a substantial amount of OPN expressing myeloid cells was themselves CD44 positive (Fig.6a-c). In fact, the number of Iba1$^+$/CD44$^+$/OPN$^+$ triple positive myeloid cells was significantly higher in the perilesional GM (142.0±47.5/mm^2) as compared to the corresponding GM in the hemisphere contralateral to infarction (1.8±2.4/mm^2) or in the GM of Sham operated rats (2.3±2.6/mm^2). Likewise, more Iba1$^+$/CD44$^+$/OPN$^+$ cells were identified in the perilesional WM (183.05±133.3/mm^2) as compared to the WM contralateral to infarction (2.4±3.02/mm^2) and the comparison to Sham WM (3.1±2.6/mm^2) approached statistical significance. Of note, a considerable proportion of CD44 positive myeloid cells was undergoing mitosis within the perilesional zone (Suppl.Fig.13a-c). Statistical comparison of all subsets within all ROIs is reported in Suppl.data.file.7. Interestingly, the spatial association of OPN positive myeloid cells to bordering CD44 positive cells was also observed in human cerebral infarctions in the stage of advanced macrophage resorption (Suppl.Fig.14a-d).

Osteopontin induces OPC migration but not proliferation *in vitro*

Osteopontin to CD44 signaling ranged among the most robust inferred immunoglial cell-cell interaction events in our dataset (Suppl.Figs.11,12). Importantly, increased cellular motility and migration are well-established functional consequence of osteopontin -> CD44 signaling in multiple cell populations [27, 56]. Interestingly, we observed that OPN positive myeloid cells and CD44 positive neuroglia accumulated at the perilesional zone in close proximity *in situ* (Fig.6). We thus speculated that OPN might increase the migratory capacity of neuroglial cells. Indeed, OPN was shown to induce migration in astrocytes *in vitro* [95]. We wondered whether OPN exerts similar effects on OPCs, which was thus far not shown. A cell gap migration assay revealed that the number of OPCs which migrated into the central gap was significantly increased upon OPN treatment (Fig.7a). To exclude that the increased cell number

964 within the central gap 48h after OPN treatment was caused by enhanced cell
965 proliferation we quantified Ki67 positive cells. The number of Ki67 positive cells within
966 the central gap did not differ significantly between OPN treated and untreated OPCs
967 (Fig.7a). We followed up on this observation using a BrdU incorporation assay, as a
968 more sensitive measurement of cell proliferation. Consistently, OPN did not increase
969 the percentage of BrdU positive cells (Fig.7b). In summary, OPN induces migration but
970 not proliferation of OPCs *in vitro*.

971

972 Discussion

973 Reactive astrogliosis is an extensively researched hallmark of the brain´s wound
974 healing response following cerebral ischemia [86, 101]. Comparatively, the response
975 of oligodendrocyte lineage cells to ischemic stroke has been less extensively
976 interrogated. Moreover, the phenotypic heterogeneity within each neuroglial
977 subpopulation and their molecular cross talk upon ischemic injury are insufficiently
978 understood, impeding a holistic perspective on the pathobiology of ischemic stroke.
979 Here we addressed these challenges by generating a large scale single cell resolution
980 transcriptomic dataset of the mammalian brain´s acute response to ischemic stroke.

981 Overall, neuroglial clusters emerged as the most transcriptionally perturbed cell
982 populations within our dataset. Within the oligodendrocyte lineage we detected two
983 transcriptional cell states which were almost uniquely detected within infarcted
984 hemispheres. In line with previous observations [14, 45], we found proliferating OPCs
985 at the perilesional zone of the infarcted hemisphere. However, beyond cell cycle
986 progression the transcriptome of these cells indicated the activation of multiple
987 survival, migration, ECM interaction and growth factor related pathways. This
988 observation suggests pleiotropic roles of OPCs during the brains wound healing
989 response to ischemic injury. Indeed, although oligodendrogenesis and hence
990 contribution to myelination are historically the most prominently described features of
991 OPCs, they are increasingly realized to have more multifaceted roles, particularly in
992 response to injury [99].

993 The second infarction associated oligodendrocyte cell state occupied a unique branch
994 at the opposite edge of the oligodendrocyte developmental trajectory. Remarkably,
995 these oligodendrocytes also upregulated the immature oligodendrocyte marker BCAS-

1 and expressed several cell-cell and cell-ECM interaction associated genes, typically enriched in immature oligodendrocytes. This observation might indicate an incomplete ischemic injury induced reacquisition of immature oligodendrocytes features in a subset of mature oligodendrocytes, a speculation necessitating further investigation. Interestingly, we did not detect a clear myelination associated gene signature within these cells. On the contrary, several myelin genes (e.g. *Mobp*, *Mbp*) were subtly downregulated and the inferred activity of several myelination and differentiation associated TFs was decreased in these cells, as compared to homeostatic mature oligodendrocytes. This observation suggests either that these oligodendrocytes are not yet fully devoted to remyelination at this early post ischemic time point, or that they assume alternative functions during the ischemic wound healing progression. As we have only sampled brain tissue 48h post injury, our study is not suited to answer this question conclusively, inviting further investigations. Importantly, recent research has demonstrated a limited and aberrant remyelination capacity of oligodendrocytes surviving demyelination compared to newly formed, progenitor derived oligodendrocytes [70]. We therefore propose that future work elucidating the potentially divergent fates and remyelination capacities of OPCs and *a priori* mature oligodendrocytes, following ischemic injury will be crucial.

The transcriptional overlap between the stroke associated oligodendrocyte lineage clusters within our dataset with previously described DAO signatures was overall limited, possibly indicating a fine tuned ischemia specific injury response. However, the DAO signature reported in Pandey et al. (2022) are derived from rodent models of neurodegeneration and de-/remyelination with disease courses ranging from multiple weeks to months [73]. Thus, it is possible that the 48h post injury sampling time point in our study was too early to observe the emergence of a more prominent DAO-like signature. Moreover, other diverging neurodegeneration associated DAO signatures have been reported and contain further partial overlaps to the stroke associated oligodendrocyte lineage cells in our dataset [48], for example regarding the upregulation of interleukin 33 (*Il33)*. However, within our sample *Il33* was not upregulated in mature stroke associated oligodendrocyte but robustly delineated stroke associated OPC in our snRNAseq dataset, as well as *in situ*. Importantly, Il33 was shown to exert neuroprotective effects during cerebral ischemia via ST2 mediated immunomodulatory signalling onto microglia and regulatory T cells [60, 100]. Moreover, Il33 was implicated in the physiological progression of OPCs to mature

oligodendrocytes [92]. The upregulation of Il33 in OPCs during cerebral ischemia might hence be involved in multiple neuroprotective pathways.

The majority of reactive astrocytes within our dataset upregulated gene sets associated to BBB maintenance, migration, cell-cell and ECM interaction, in line with previous work [13, 80]. This transcriptional profile corresponds well to the canonical roles of astrocytes in ECM scaffold formation and spatial containment of the neurotoxic core lesions microenvironment following CNS injury [86]. As expected, the reactive astrocyte signatures within our dataset overlapped with the canonical ischemia associated A2-signature, but not with the inflammation induced A1-signature [59, 103]. Interestingly, the stroke reactive astrocyte transcriptomes in our dataset overlapped partially with MS “reactive/stressed astrocytes” [1] and neurodegeneration associated DAA signatures [36], highlighting common astrocyte responses to diverse neuronal injuries. Notably, we identified a small, predominantly severe infarction derived, subset of reactive astrocytes (AC_5), characterized by an upregulation of primary cilium associated genes. Intriguingly, a similar enrichment of primary cilium associated genes was previously identified in reactive astrocyte subsets in MS and Parkinson’s disease [1, 78]. Furthermore, Wei et al. have recently characterized a population of astrocyte-ependymal cells in spinal cord tissue which expanded after acute injury [97]. This population shared several transcriptional similarities with the reactive AC_5 subcluster in our dataset such as the upregulation of *Rfx3* and Dnah encoding genes and increased Foxj1 TF activity. The precise origin and function of cilia gene enriched or astrocyte-ependymal cell states in response to CNS injuries are still largely unknown. Astrocytes and ependymal cells are developmentally closely related and they form a common transcriptional taxon [104]. Limited by the low number of captured AC_5 nuclei and the single sampling time point in our study, we can thus far not conclude whether the expansion of the AC_5 cluster upon MCAO was caused by the acquisition of ependymal cell features by astrocytes, upregulation of reactive astrocytes genes in ependymal cells, or both. Further studies will be necessary to unveil the elusive role of these cells in ischemic stroke and other neuropathologies.

Under physiological conditions astrocytes are crucially involved in the regulation of ion and neurotransmitter signalling, as well as synapse assembly and maintenance [96]. Our findings indicate a possible loss of these homeostatic functions in stroke reactive astrocytes. Likewise, oligodendrocyte lineage cells are increasingly recognized to be

coupled to neuronal neurotransmitter signalling via bidirectional cross talk, at OPC and axo-myelinic synapses [68, 99]. Interestingly, similarly to astrocytes, multiple neurotransmitter receptors, ion channels and ion channel interacting proteins were downregulated in oligodendrocyte lineage cells upon cerebral ischemia. Some of these genes were also downregulated subtly in the hemisphere contralateral to infarction. Further studies will be necessary to assess whether these changes functionally relate to possible disruptions of homeostatic oligodendroglia-neuronal crosstalk.

While comparing the cerebral ischemia induced transcriptional perturbations in oligodendrocyte lineage cells and astrocytes we noticed further, more prominent similarities between infarction restricted oligodendrocyte lineage and astrocyte populations. Similar to reactive astrocytes, infarction restricted OPCs upregulated migration, cell-cell and ECM-interaction genes (e.g. *Met*, *Cdh2*, *Tnc*, *Adamts1*, *Adamts9*, *Vim*, *Cd44*) and colocalized with reactive astrocytes at the perilesional zone. It is thus possible that the perilesional microenvironment instructs a shared phenotype onto these populations. The partial acquisition of reactive astrocyte associated genes in oligodendrocytes after injury has also been noted in previous studies. Importantly, Kirdajova et al. have documented the emergence of a stroke specific, transient, proliferating “Astrocyte-like NG2 glia” population seven days after focal cerebral ischemia and speculated that this population might contribute to early glial scar formation [50]. Although, a subset of OPCs progresses to myelinating oligodendrocytes following ischemic stroke particularly in young animals [45], a substantial amount of OPCs remains undifferentiated for up to eight weeks post injury, suggesting potential alternative cell fates [14].

More recently it was also shown that *bona fide* mature oligodendrocytes can dedifferentiate via a hybrid “AO cell” state into astrocytes *in vivo*, in the days to weeks following traumatic and ischemic brain injury [7]. This phenotypic switch was causally linked to IL6 signalling. Interestingly, the infarction enriched mature oligodendrocytes in our dataset would be primed to respond to this cytokine due to the prominent upregulation of canonical downstream targets of IL6, such as *Il6st* and *Stat3*. However, the transcriptional similarities between reactive OPCs, oligodendrocytes and astrocyte cluster within our datasets do not necessarily indicate that they harbour the progeny of hybrid cell states. Moreover, overlaps in gene and TF signatures do not unequivocally dictate shared functions during neural regeneration. For example, traumatic injury

induced STAT3 activation in astrocytes is involved in GFAP upregulation, induction of cellular hypertrophy and glial scar formation [40], while in oligodendrocytes STAT3 signalling was implicated in maturation and remyelination after focal demyelination [91]. Further studies will be necessary to decipher the precise functional consequences of the herein described gene expressional changes in oligodendroglia and astrocytes.

The recruitment of reactive neuroglia and immune cells to the injury site is a crucial step during the acute ischemic injury response [23]. Our data indicate that myeloid cells might be involved in orchestrating this process. We confirmed the emergence of SAMC specifically within infarcted brain tissue. The sparsity of myeloid cells within non-lesioned brain tissue is a previously elaborated [15] limitation of our nuclei isolation approach and impeded a direct comparison of SAMC to homeostatic microglia within this study, which has already been conducted elsewhere [10]. Although the herein used method of nuclei isolation is prone to exclude immune cells, they were robustly captured within infarcted tissue, highlighting their drastically increased abundance in the infarct lesion. The clearance of lipid-rich tissue debris has been established as a primary function of SAMC [10], although alternative functions, such as the reduction of ROS stress, have been described [49]. Here we observed that myeloid cells expressing the canonical SAMC marker osteopontin accumulate in close proximity to reactive astrocytes and proliferating OPCs which robustly expressed the osteopontin receptor CD44 in the perilesional zone. Furthermore, we were able to show that osteopontin increased the migratory capacity of OPCs *in vitro*. Indeed, osteopontin is a well-established inductor of cellular migration in numerous cell types and has been implicated to act as a chemotactic cue via CD44 mediated signalling [56, 95]. In addition, CD44 was shown to be indispensable for the migration of transplanted rat OPC-like CG4 cells towards focal demyelinated lesions [74], and macrophage derived osteopontin was shown to induce the extension of astrocyte processes towards the infarct perilesional zone following focal cerebral ischemia [33]. The accumulation of CD44 positive astrocytes and immune cells in the peri-infarct zone was previously shown and associated to a homing towards the CD44 ligand hyaluronic acid, which also accumulates at the peri-infarct border [2, 3, 83]. Importantly, our CCC analysis inferred that CD44 is indeed targeted by multiple ligands in infarcted tissue specifically. Likewise, osteopontin was predicted to signal onto multiple other receptors, such as integrins which was previously also associated to increased migration [106]. As the recruitment of neuroglia and immune cells to the site of injury is a prerequisite for

further regenerative mechanisms, it is highly plausible that multiple redundant mechanisms have evolved to achieve this. Moreover, the role of osteopontin in ischemic stroke likely exceeds the regulation of cellular migration, although its precise contribution to post ischemic regeneration is still controversial. For example, osteopontin has been shown to acutely aggravate ischemia-induced BBB disruption [90], but augment white matter integrity via immunomodulatory mechanisms, in the subacute to chronic stages of stroke recovery [87]. A further complicating factor is the age dependency of many molecular cross talk events during the response to cerebral ischemia. For example, osteopontin to CD44 signaling was largely restricted to young animals in a previous study [45]. The fact that our results are based on a homogenous cohort of young, male rats is an evident limitation that has to be taken into account when extrapolating translational considerations from this dataset.

In summary, our study captured the emergence of cell type and cerebral infarction specific transcriptional signatures in neuroglia. Although, reactive oligodendrocyte lineage cells and astrocytes exhibited distinct responses their transcriptional signatures overlapped substantially, indicating a shared molecular ischemia response repertoire and possibly shared functions during regeneration. Moreover, we uncovered a shared immuno-glial molecular cross talk, which implicated myeloid cells as contributors to OPC and reactive astrocyte recruitment to the injury site via the osteopontin CD44 signaling axis. Beyond the diverse transcriptional response patterns highlighted in our analysis, the large scale dataset generated within this study will provide an instrumental resource for the interrogation of acute cell type specific responses to ischemic stroke. We propose, that this approach will contribute to untangle the complex mechanisms governing post ischemic neural regeneration, ultimately aiding in the discovery of novel treatment strategies to alleviate the devastating consequences of ischemic stroke.

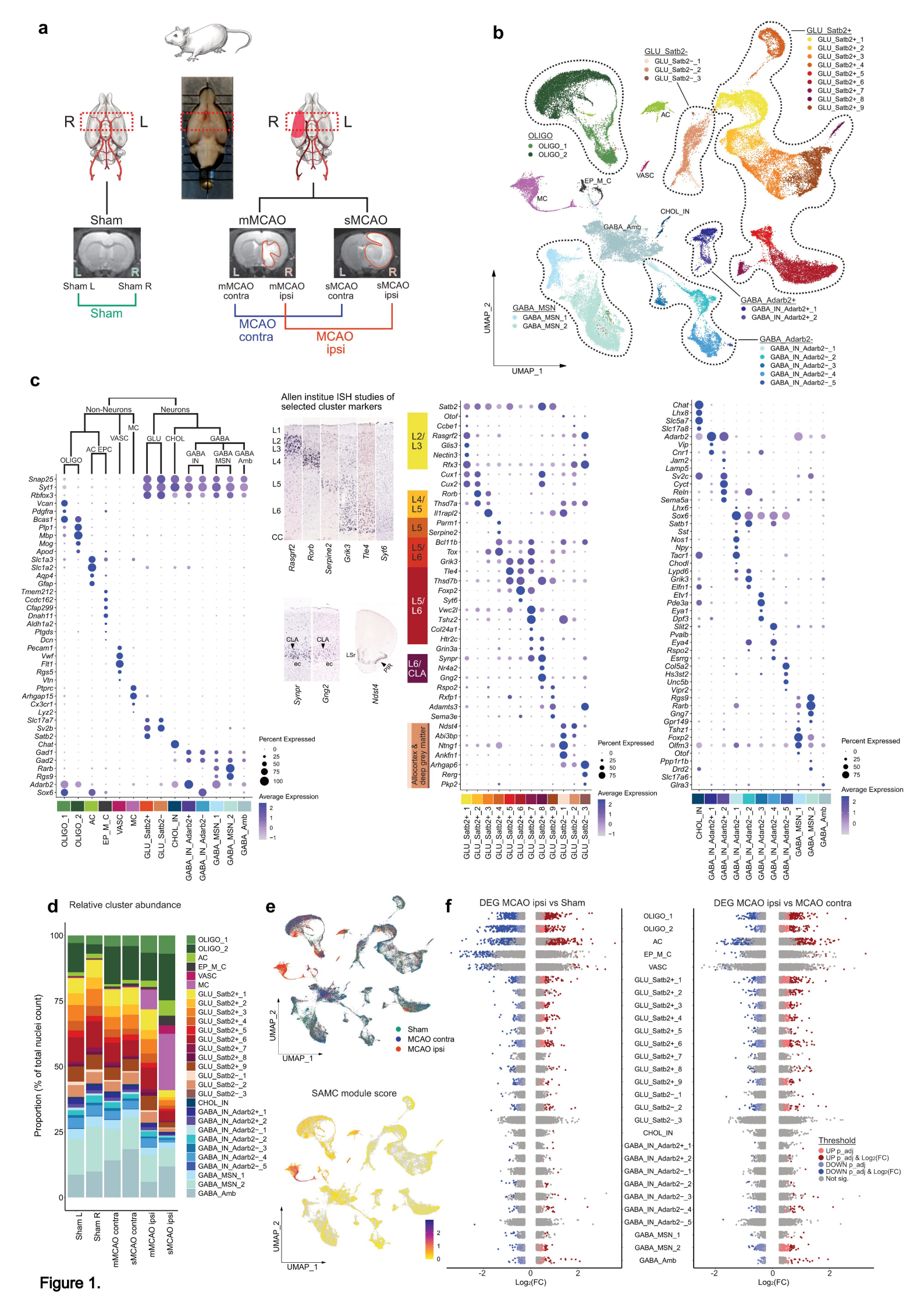
a
R
L
Sham
Sham L
Sham R
Sham
mMCAO
sMCAO
mMCAO contra
mMCAO ipsi
sMCAO contra
sMCAO ipsi
MCAO contra
MCAO ipsi
b
GLU_Satb2+
GLU_Satb2+_1
GLU_Satb2+_2
GLU_Satb2+_3
GLU_Satb2+_4
GLU_Satb2+_5
GLU_Satb2+_6
GLU_Satb2+_7
GLU_Satb2+_8
GLU_Satb2+_9
GLU_Satb2-
GLU_Satb2-_1
GLU_Satb2-_2
GLU_Satb2-_3
AC
VASC
OLIGO
OLIGO_1
OLIGO_2
EP_M_C
MC
CHOL_IN
GABA_Amb
GABA_MSN
GABA_MSN_1
GABA_MSN_2
GABA_Adarb2+
GABA_IN_Adarb2+_1
GABA_IN_Adarb2+_2
GABA_Adarb2-
GABA_IN_Adarb2-_1
GABA_IN_Adarb2-_2
GABA_IN_Adarb2-_3
GABA_IN_Adarb2-_4
GABA_IN_Adarb2-_5
UMAP_1
UMAP_2
c
Non-Neurons
Neurons
OLIGO
AC EPC
MC
VASC
GLU
CHOL
GABA
GABA IN
GABA MSN
GABA Amb
Allen institue ISH studies of selected cluster markers
L1
L2
L3
L4
L5
L6
CC
Rasgrf2
Rorb
Serpine2
Grik3
Tle4
Syt6
CLA
ec
LSr
PIR
Synpr
Gng2
Ndst4
L2/ L3
L4/ L5
L5
L5/ L6
L5/ L6
L6/ CLA
Allocortex & deep grey matter
Percent Expressed
Average Expression
d
Relative cluster abundance
Proportion (% of total nuclei count)
Sham L
Sham R
mMCAO contra
sMCAO contra
mMCAO ipsi
sMCAO ipsi
e
Sham
MCAO contra
MCAO ipsi
SAMC module score
f
DEG MCAO ipsi vs Sham
DEG MCAO ipsi vs MCAO contra
Log2(FC)
Threshold
UP p_adj
UP p_adj & Log2(FC)
DOWN p_adj
DOWN p_adj & Log2(FC)
Not sig.

Figure 1.

Figure 1. snRNAseq reveals differential cell cluster abundance and cluster specific transcriptional perturbations 48h after ischemic stroke. (a) Illustration of study design, depicting brain regions sampled for snRNAseq, from n=4 Sham control rats and n=7 MCAO rats. MRI images of brain tissue from Sham operated, mMCAO and sMCAO rats are presented, ischemic lesions are highlighted in red. **(b)** UMAP plot depicting 68616 nuclei annotated to 29 major cell clusters in the overall integrated dataset. Cell cluster abbreviations: AC: astrocyte cluster, CHOL_IN: cholinergic interneurons, EP_M_C: ependymal and mural cell cluster, GABA_Amb: Ambiguous GABAergic neuronal cluster, GABA_IN_Adarb2+, GABA_IN_Adarb2-: GABAergic interneurons, *Adarb2* positive/negative, respectively, GABA_MSN: GABAergic medium spiny neurons, GLU_Satb2+, GLU_Satb2-: Glutamatergic neurons, *Satb2* positive/negative, respectively, OLIGO_1: immature oligodendrocyte lineage cluster, OLIGO_2: myelinating and mature oligodendrocyte lineage cluster. **(c)** Dotplots depicting curated marker genes for all major cell clusters. The dendrogram on top of the left dotplot represents overarching taxons of identified major cell clusters. The dotplot in the middle depicts curated cluster markers of glutamatergic neurons. Colored bars next to the gene names denote established associations to cortical layers. Representative corresponding RNA in situ hybridization (ISH) results are depicted next to the colored bars. All RNA ISH studies were taken from Allen Brain Atlas database [57], and are referenced in detail in Suppl.Tab.3. Abbreviations: L = layer, CLA = claustrum, ec = external capsule, LSr = lateral septal nucleus, PIR = piriform cortex. Dotplot on the right shows marker gene expression in cholinergic and GABAergic neurons. **(d)** Stacked bar plot depicting the relative abundance of each cell cluster within each sample. **(e)** Top: Nuclei distribution coloured by treatment group. Bottom: Gene module score derived from the stroke-associated myeloid cell (SAMC) gene set [10]. **(f)** Strip plots depicting distribution of DEGs derived from MCAO ipsi vs Sham and MCAO ipsi vs MCAO contra comparisons, for all major cell clusters.

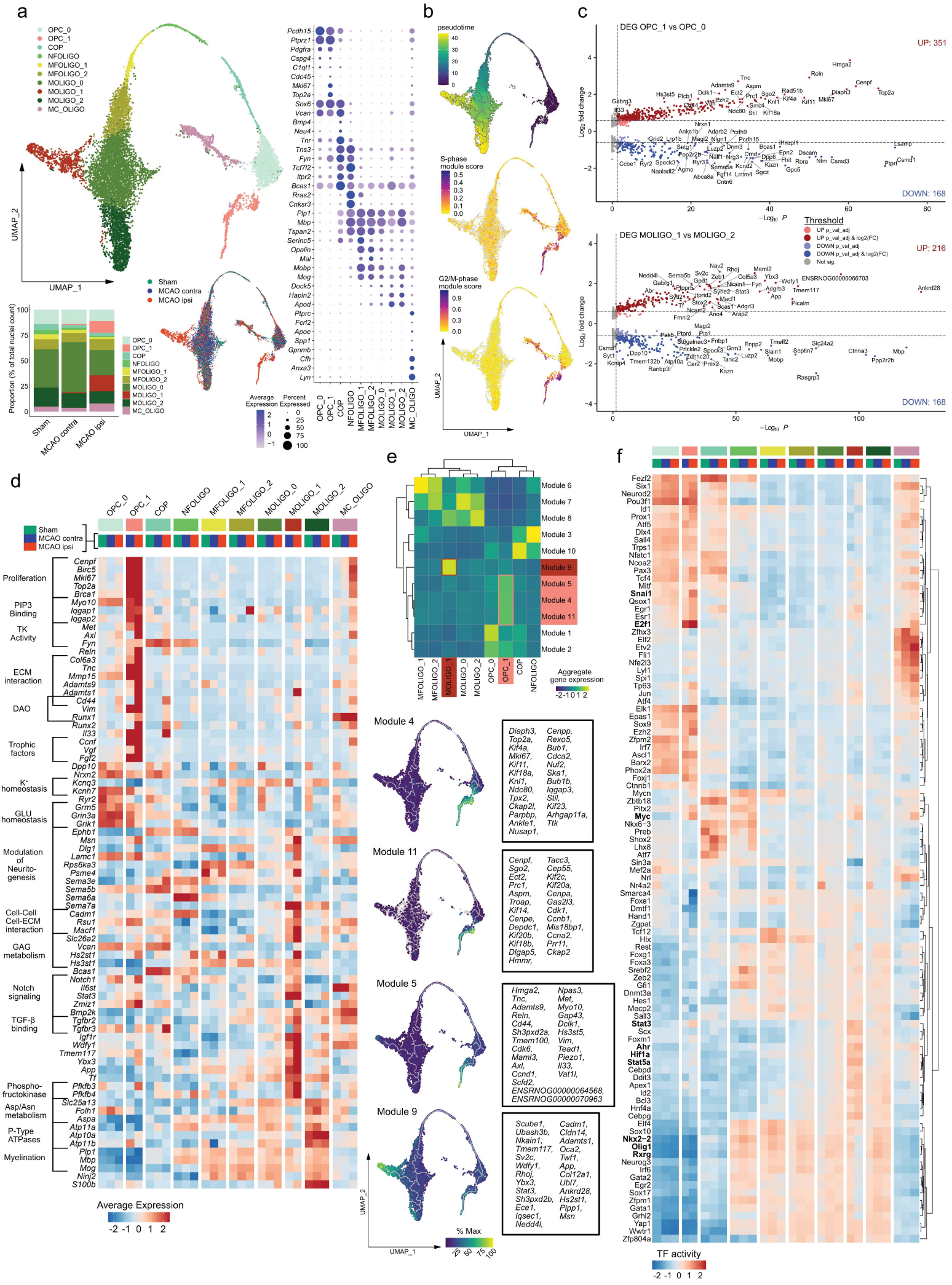
a
OPC_0
OPC_1
COP
NFOLIGO
MFOLIGO_1
MFOLIGO_2
MOLIGO_0
MOLIGO_1
MOLIGO_2
MC_OLIGO
UMAP_1
UMAP_2
Sham
MCAO contra
MCAO ipsi
Proportion (% of total nuclei count)
Average Expression
Percent Expressed
b
pseudotime
S-phase module score
G2/M-phase module score
c
DEG OPC_1 vs OPC_0
UP: 351
DOWN: 168
DEG MOLIGO_1 vs MOLIGO_2
UP: 216
DOWN: 168
Log2 fold change
Threshold
UP p_val_adj
UP p_val_adj & log2(FC)
DOWN p_val_adj
DOWN p_val_adj & log2(FC)
Not sig.
d
Proliferation
PIP3 Binding
TK Activity
ECM interaction
DAO
Trophic factors
K+ homeostasis
GLU homeostasis
Modulation of Neurito-genesis
Cell-Cell Cell-ECM interaction
GAG metabolism
Notch signaling
TGF-β binding
Phospho-fructokinase
Asp/Asn metabolism
P-Type ATPases
Myelination
Average Expression
e
Module 6
Module 7
Module 8
Module 3
Module 10
Module 9
Module 5
Module 4
Module 11
Module 1
Module 2
Aggregate gene expression
Module 4
Diaph3, Top2a, Kif4a, Mki67, Kif11, Kif18a, Knl1, Ndc80, Tpx2, Ckap2l, Parpbp, Ankle1, Nusap1, Cenpp, Rexo5, Bub1, Cdca2, Nuf2, Ska1, Bub1b, Iqgap3, Stil, Kif23, Arhgap11a, Ttk
Module 11
Cenpf, Sgo2, Ect2, Prc1, Aspm, Troap, Kif14, Cenpe, Depdc1, Kif20b, Kif18b, Dlgap5, Hmmr, Tacc3, Cep55, Kif2c, Kif20a, Cenpa, Gas2l3, Cdk1, Ccnb1, Mis18bp1, Ccna2, Prr11, Ckap2
Module 5
Hmga2, Tnc, Adamts9, Reln, Cd44, Sh3pxd2a, Tmem100, Cdk6, Maml3, Axl, Ccnd1, Scfd2, ENSRNOG00000064568, ENSRNOG00000070963, Npas3, Met, Myo10, Gap43, Dclk1, Hs3st5, Vim, Tead1, Piezo1, Il33, Vat1l,
Module 9
Scube1, Ubash3b, Nkain1, Tmem117, Sv2c, Wdfy1, Rhoj, Ybx3, Stat3, Sh3pxd2b, Ece1, Iqsec1, Nedd4l, Cadm1, Cldn14, Adamts1, Oca2, Twf1, App, Col12a1, Ubl7, Ankrd28, Hs2st1, Plpp1, Msn
% Max
f
TF activity

Figure 2.

Figure 2. Emergence of transcriptionally distinct OPCs and mature oligodendrocytes within infarcted brain tissue. (a) Subclustering of oligodendrocyte lineage clusters. Top left: UMAP plot depicting 10240 nuclei annotated to 10 subclusters, bottom left: stacked bar plot depicting the relative abundance of each subcluster within each group, bottom right: Nuclei distribution coloured by treatment group, right panel: dotplot depicting curated sub cluster markers. Subcluster abbreviations: OPC: oligodendrocyte precursor cell, COP: committed oligodendrocyte precursor, NFOLIGO: newly formed oligodendrocyte, MFOLIGO: myelin forming oligodendrocyte, MOLIGO: mature oligodendrocyte, MC_OLIGO: myeloid cell oligodendrocyte mixed cluster. **(b)** Top: Projection of Monocle3 generated pseudotime trajectory onto subcluster UMAP plot, with subcluster OPC_0 as root. Feature Plots depicting S-phase (middle) and G2/M-phase (bottom) gene module scores. **(c)** Volcano plots depicting DEGs derived from the comparison of clusters OPC_1 to OPC_0 (top) and MOLIGO_1 to MOLIGO_2 (bottom). **(d)** Heatmap depicting the average scaled gene expression of curated DEGs, split by subcluster and treatment group. Functional annotations are given on the left side of the gene names. **(e)** Top: Clustered heatmap depicting aggregate gene expressions of Monocle3 derived co-regulated gene modules. Modules associated to OPC_1 and MOLIGO_1 are highlighted in light and dark red, respectively. Bottom: The average aggregate expression of the OPC_1 and MOLIGO_1 associated modules is plotted along the pseudo time trajectory. The Top 25 module defining genes, as sorted by descending Moran´s I, are depicted in boxes on the right side of the respective gene module feature plots. **(f)** Heatmap depicting the top 100 most variable decoupleR derived transcription factor activities, within the oligodendrocyte lineage sub clustering analysis, split by sub cluster and treatment group.

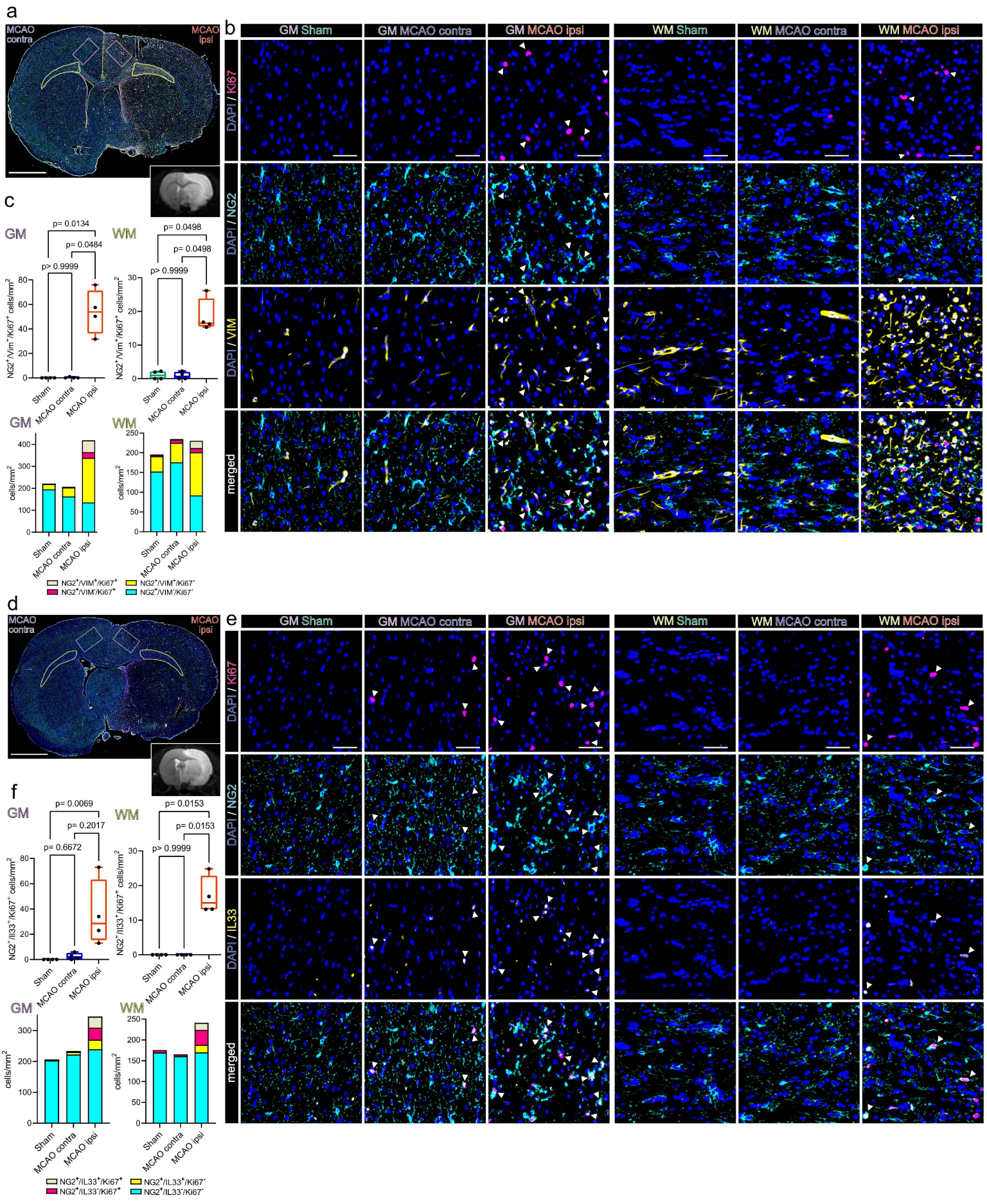

1303 **Figure 3.**

1304

Figure 3. Proliferating OPCs accumulate in the perilesional zone 48 h after ischemic stroke and express VIM and IL33. (a) Overview of a representative coronal brain section 48 h post MCAO, stained for NG2, VIM and Ki67. Grey matter ROIs (GM) are highlighted in violet, white matter ROIs (WM) in lime green, lower right inset depicts a corresponding T2 weighted MRI image from the same animal. Bar = 2 mm **(b)** Representative images from GM and WM ROIs of Sham, MCAO contra and MCAO ipsi sections, split by antigen. Ki67 = magenta, NG2 = Cyan, VIM = yellow, DAPI (nuclei) = blue, bars = 50 µm. White arrowheads point to triple positive cells. **(c)** Cell counts within GM and WM respectively are presented as box plots for $NG2^+/VIM^+/Ki67^+$ triple positive cells. Cell counts for $NG2^+/VIM^+/Ki67^+$, $NG2^+/VIM^-/Ki67^+$, $NG2^+/VIM^+/Ki67^-$, $NG2^+/VIM^-/Ki67^-$ are also jointly shown as colored stacked bar plot. **(d)** Representative coronal overview, 48 h post MCAO, stained for NG2, IL33, Ki67. GM ROIs in violet, WM ROIs in lime green, lower right inset shows a corresponding MRI image from the same animal. Bar = 2 mm **(e)** Representative images from GM and WM ROIs derived from Sham, MCAOcontra and MCAOipsi groups, split by antigen. Ki67 = magenta, NG2 = Cyan, IL33 = yellow, DAPI (nuclei) = blue, bars = 50 µm White arrowheads point to triple positive cells. **(f)** Cell counts within GM and WM are presented as box plots for $NG2^+/IL33^+/Ki67^+$ triple positive cells. Cell counts for $NG2^+/IL33^+/Ki67^+$, $NG2^+/IL33^-/Ki67^+$, $NG2^+/IL33^+/Ki67^-$, $NG2^+/IL33^-/Ki67^-$ are also jointly shown as colored stacked bar plot. Data derived from n = 4-5 animals per group, p values derived from Kruskal-Wallis-H-Tests, followed by Dunn's post hoc comparisons.

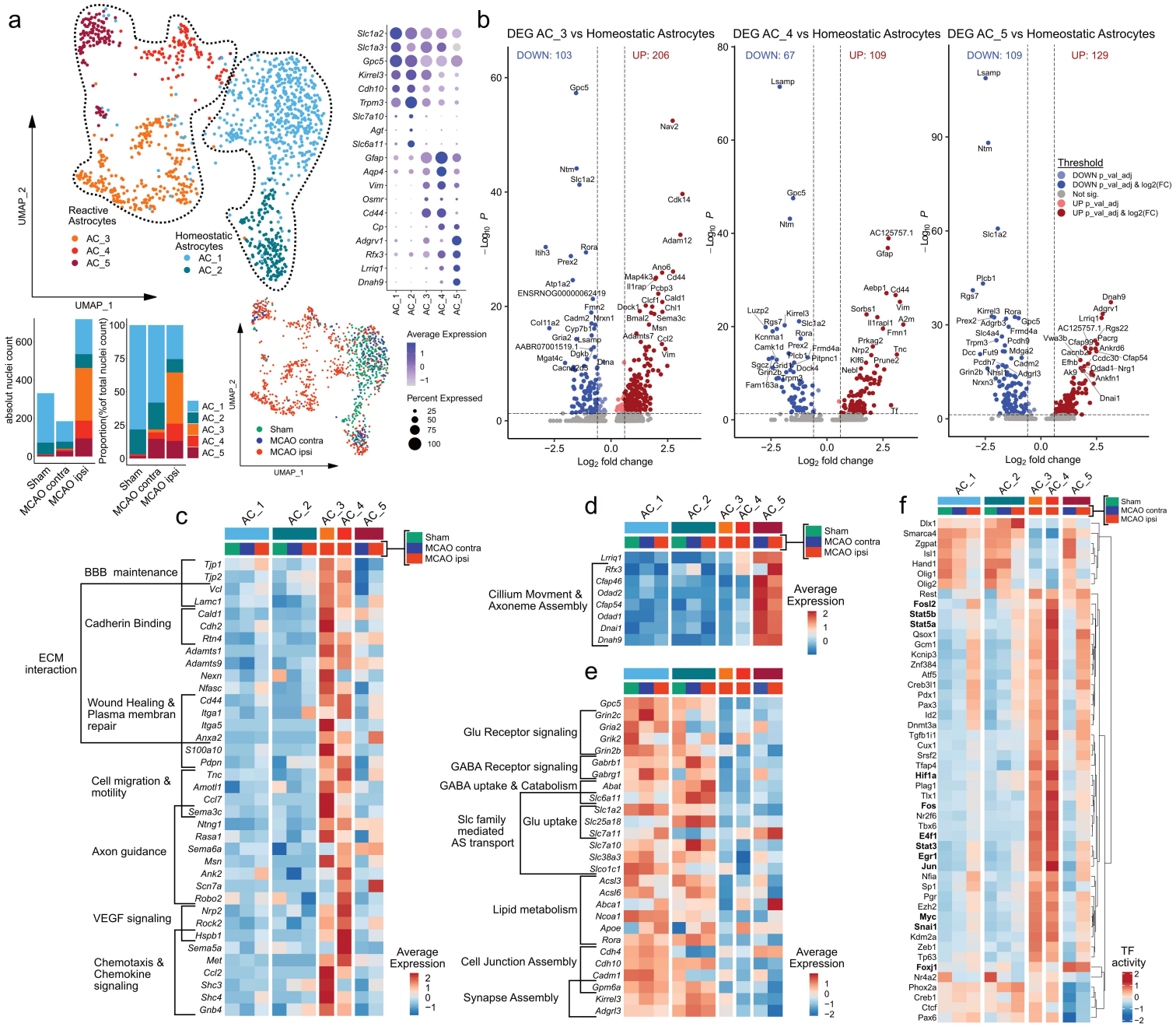
a
UMAP_2
UMAP_1
Reactive Astrocytes
AC_3
AC_4
AC_5
Homeostatic Astrocytes
AC_1
AC_2
Slc1a2
Slc1a3
Gpc5
Kirrel3
Cdh10
Trpm3
Slc7a10
Agt
Slc6a11
Gfap
Aqp4
Vim
Osmr
Cd44
Cp
Adgrv1
Rfx3
Lrriq1
Dnah9
Average Expression
Percent Expressed
absolut nuclei count
Proportion(%of total nuclei count)
Sham
MCAO contra
MCAO ipsi
b
DEG AC_3 vs Homeostatic Astrocytes
DOWN: 103
UP: 206
DEG AC_4 vs Homeostatic Astrocytes
DOWN: 67
UP: 109
DEG AC_5 vs Homeostatic Astrocytes
DOWN: 109
UP: 129
Threshold
DOWN p_val_adj
DOWN p_val_adj & log2(FC)
Not sig.
UP p_val_adj
UP p_val_adj & log2(FC)
−Log10 P
Log2 fold change
c
ECM interaction
BBB maintenance
Cadherin Binding
Wound Healing & Plasma membran repair
Cell migration & motility
Axon guidance
VEGF signaling
Chemotaxis & Chemokine signaling
d
Cillium Movment & Axoneme Assembly
e
Glu Receptor signaling
GABA Receptor signaling
GABA uptake & Catabolism
Slc family mediated AS transport
Glu uptake
Lipid metabolism
Cell Junction Assembly
Synapse Assembly
f
TF activity

Figure 4.

Figure 4. Transcriptional heterogeneity of reactive astrocytes within infarcted brain tissue. (a) Subclustering analysis of astrocytes. Top left: UMAP plot depicting 1233 nuclei annotated to 5 subclusters, bottom left: stacked bar plots depicting the absolute and relative abundance of each subcluster within each group, bottom right: Nuclei distribution coloured by group, right panel: Dotplot depicting curated homeostatic and reactive astrocyte marker genes. **(b)** Volcano plots depicting DEG derived from the comparison of the reactive astrocyte subclusters AC_3 (left), AC_4 (middle) and AC_5 (right) to the homeostatic astrocyte subclusters (AC_1 and AC_2, pooled). **(c-f)** Heatmaps depicting the average scaled gene expression of curated upregulated DEGs, derived from the comparison of AC_3 and AC_4 **(c)** and AC_5 **(d)** to homeostatic astrocytes, as well as DEGs downregulated in reactive astrocytes **(e)**, split by subcluster and group. **(f)** Clustered heatmap depicting the top 50 most variable decoupleR derived transcription factor activities, within the astrocyte lineage subclustering analysis, split by subcluster and treatment group.

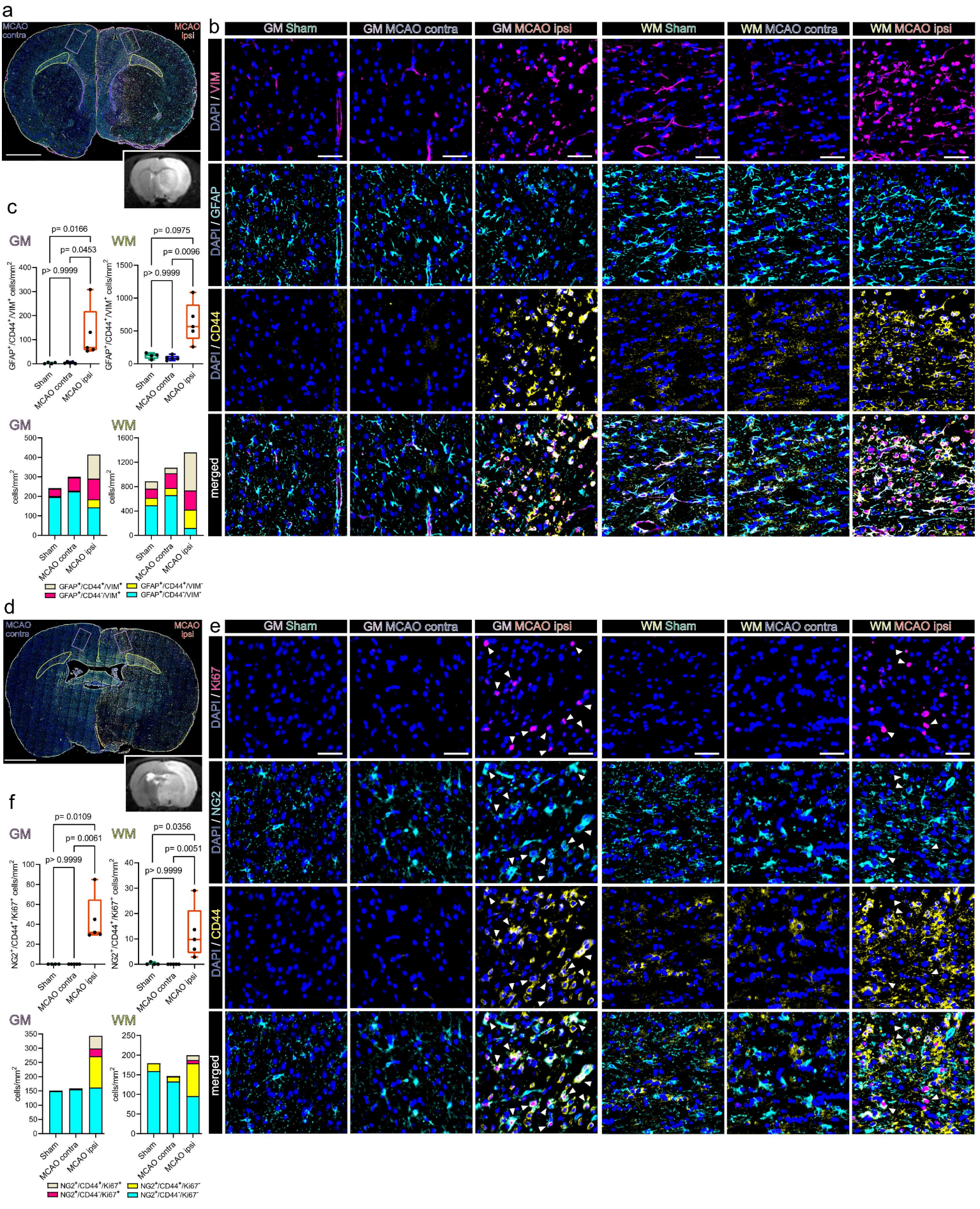

1411 **Figure 5.**

Figure 5. Reactive astrocytes and proliferating OPCs are CD44 positive and abundant in the perilesional zone 48 h after ischemic stroke. (a) Overview of a representative coronal brain section 48 h post MCAO, stained for GFAP, CD44 and VIM. Grey matter ROIs (GM) are highlighted in violet, white matter ROIs (WM) in lime green, lower right inset depicts a corresponding T2 weighted MRI image from the same animal. Bar = 2mm **(b)** Representative images taken from GM and WM ROIs of Sham, MCAO contra and MCAO ipsi sections, split by antigen. VIM = magenta, GFAP = Cyan, CD44 = yellow, all overlaid with DAPI (nuclei) = blue. Bars = 50 µm. White arrowheads point to NG2+/CD44+/Ki67+ triple positive cells. **(c)** Cell counts within GM and WM are presented as box plots for $GFAP^+/CD44^+/VIM^+$ triple positive cells. Cell counts for $GFAP^+/CD44^+/VIM^+$, $GFAP^+/CD44^-/VIM^+$, $GFAP^+/CD44^+/VIM^-$, $GFAP^+/CD44^-/VIM^-$ are also jointly shown as colored stacked bar plot. **(d)** Representative coronal overview, 48 h post MCAO, stained for NG2, CD44, Ki67. GM ROIs in violet, WM ROIs in lime green, lower right inset shows corresponding MRI image from the same animal. Bar = 2mm **(e)** Representative images from GM and WM ROIs taken from Sham, MCAO contra and MCAO ipsi groups, split by antigen. Ki67 = magenta, NG2 = Cyan, CD44 = yellow. Bars = 50 µm. White arrowheads point to NG2+/CD44+/Ki67+ triple positive cells. **(f)** Cell counts within GM and WM respectively are presented as box plots for $NG2^+/CD44^+/Ki67^+$. Cell counts for $NG2^+/CD44^+/Ki67^+$, $NG2^+/CD44^-/Ki67^+$, $NG2^+/CD44^+/Ki67^-$, $NG2^+/CD44^-/Ki67^-$ are also jointly shown as colored stacked bar plot. Data derived from n = 4-5 animals per group, p values derived from Kruskal-Wallis-H-Tests, followed by Dunn's post hoc comparisons.

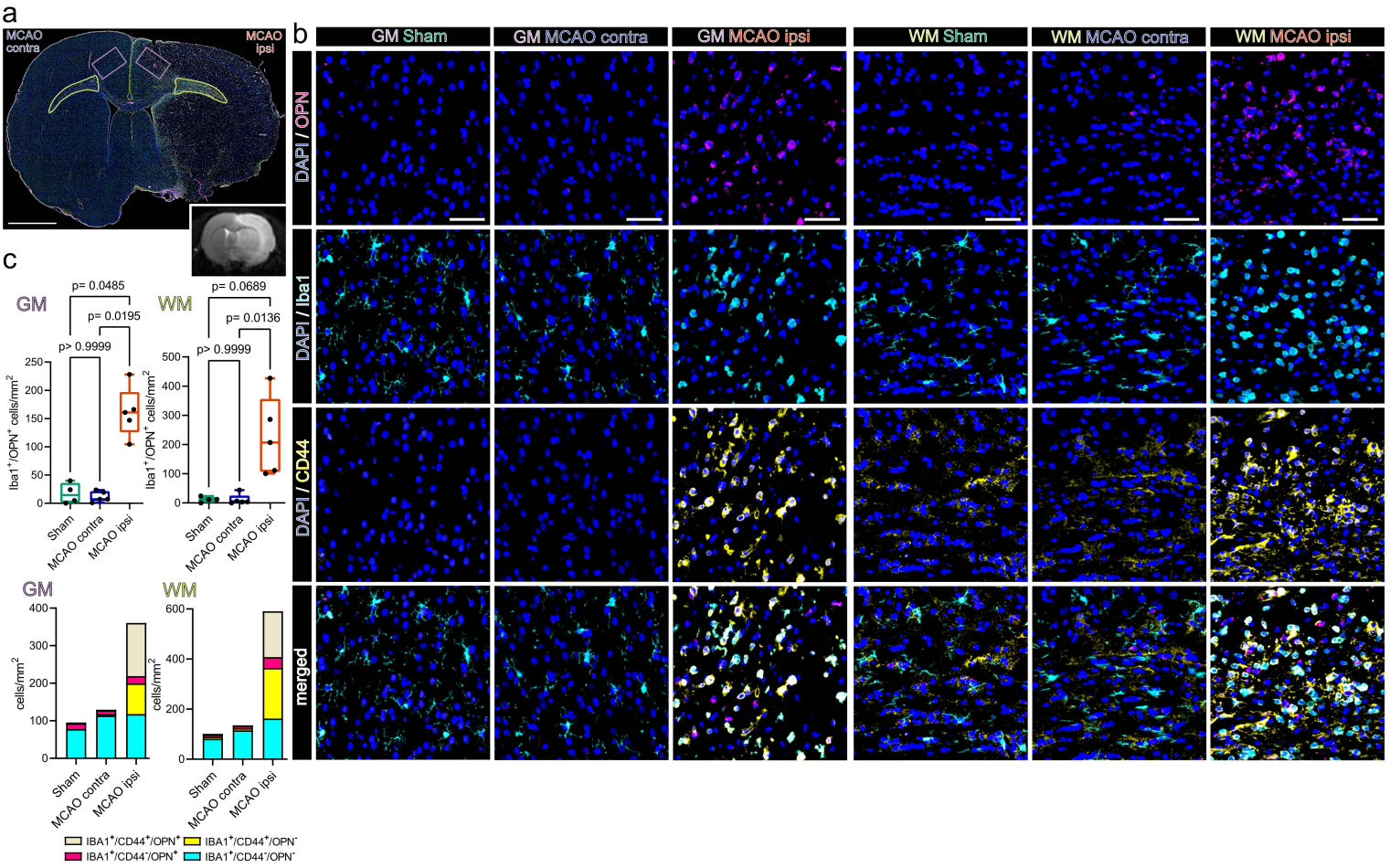
a
MCAO contra
MCAO ipsi
b
GM Sham
GM MCAO contra
GM MCAO ipsi
WM Sham
WM MCAO contra
WM MCAO ipsi
DAPI / OPN
DAPI / Iba1
DAPI / CD44
merged
c
GM
WM
p= 0.0485
p= 0.0195
p> 0.9999
p= 0.0689
p= 0.0136
p> 0.9999
Iba1+/OPN+ cells/mm2
Sham
MCAO contra
MCAO ipsi
cells/mm2
IBA1+/CD44+/OPN+
IBA1+/CD44+/OPN-
IBA1+/CD44-/OPN+
IBA1+/CD44-/OPN-

Figure 6.

Figure 6. Osteopontin positive myeloid cells accumulate in the perilesional zone in close proximity to CD44 positive cells 48 h after ischemic stroke. (a) Overview of a representative coronal brain section 48 h post MCAO, stained for Iba1, CD44 and OPN. Grey matter ROIs (GM) are highlighted in violet, white matter ROIs (WM) in lime green, lower right inset depicts a corresponding T2 weighted MRI image from the same animal. Bar = 2 mm. **(b)** Representative images from GM and WM ROIs of Sham, MCAOcontra and MCAO ipsi sections, split by antigen. OPN = magenta, Iba1 = cyan, CD44 = yellow. Bar = 50 µm. **(c)** Cell counts within GM and WM are presented as box plots for $Iba1^{+}/OPN^{+}$ double positive cells, cell counts for $Iba1^{+}/CD44^{+}/OPN^{+}$, $Iba1^{+}/CD44^{-}/OPN^{+}$, $Iba1^{+}/CD44^{+}/OPN^{-}$, $Iba1^{+}/CD44^{-}/OPN^{-}$ are jointly shown as colored stacked bar plot. Data derived from n = 4-5 animals per group, p values derived from Kruskal-Wallis-H-Tests, followed by Dunn's post hoc comparisons.

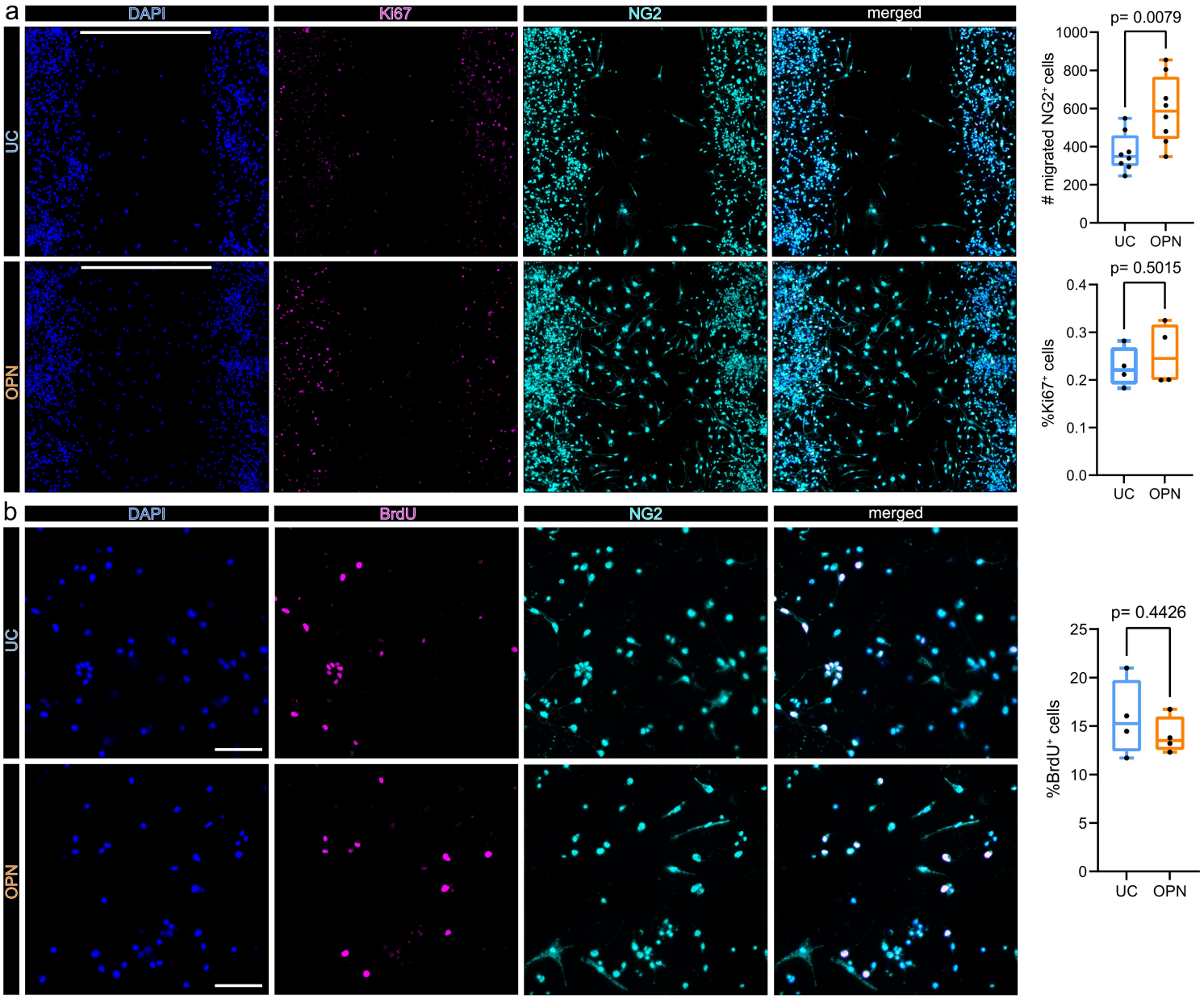
a
DAPI
Ki67
NG2
merged
UC
OPN
p= 0.0079
# migrated NG2+ cells
1000
800
600
400
200
0
UC
OPN
p= 0.5015
%Ki67+ cells
0.4
0.3
0.2
0.1
0.0
UC
OPN
b
DAPI
BrdU
NG2
merged
UC
OPN
p= 0.4426
%BrdU+ cells
25
20
15
10
5
0
UC
OPN

Figure 7.

Figure 7. Osteopontin induces OPC migration but not proliferation *in vitro*. (a) *In vitro* cell migration assay. Cells were seeded in 2 well culture inserts, creating defined 500 µm gaps. NG2 positive cells which migrated into the 500 µm gap were quantified after 48 h of treatment. Representative images of OPC cell cultures 48 h after incubation without (upper panel: untreated control = UC), or with 1 µg/ml OPN (lower panel), stained for DAPI (nuclei) = blue, Ki67 = magenta and NG2 = cyan, split by channel. Scale bars denote 500 µm gaps. Box plots on the right show the number of NG2 positive cells, which migrated into 500 µm gaps, for each condition, p-values derived from unpaired student´s t-test (t=3,097, df=14, n=8 replicates per group, from 2 independent experiments). In n = 4 replicates per group from 2 independent experiments Ki67 was visualized. Lower Boxplot depicts the percentages of $Ki67^+$ cells within the 500 µm gap, for each condition, p values derived from unpaired student´s t-test (t=0,7150, df=6). **(b)** BrdU incorporation assay. BrdU incorporation was visualized 24h after incubation without (UC) (upper panel) or with 1 µg/ml OPN (lower panel). Representative 20x magnification images are shown, stained for DAPI (Nuclei) = blue, BrdU = magenta and NG2 = cyan, split by channel. Scale bars = 100 µm. Boxplot depicts the percentages of $BrdU^+$ cells, for each group, p values derived from unpaired student´s t-test (t=0,8219, df=6, n=4 replicates per group, from 1 independent experiment).

References

1 Absinta M, Maric D, Gharagozloo M, Garton T, Smith MD, Jin J, Fitzgerald KC, Song A, Liu P, Lin JPet al (2021) A lymphocyte-microglia-astrocyte axis in chronic active multiple sclerosis. Nature 597: 709-714 Doi 10.1038/s41586-021-03892-7

2 Al'Qteishat A, Gaffney J, Krupinski J, Rubio F, West D, Kumar S, Kumar P, Mitsios N, Slevin M (2006) Changes in hyaluronan production and metabolism following ischaemic stroke in man. Brain 129: 2158-2176 Doi 10.1093/brain/awl139

3 Al Qteishat A, Gaffney JJ, Krupinski J, Slevin M (2006) Hyaluronan expression following middle cerebral artery occlusion in the rat. Neuroreport 17: 1111-1114 Doi 10.1097/01.wnr.0000227986.69680.20

4 Ali MF, Latimer AJ, Wang Y, Hogenmiller L, Fontenas L, Isabella AJ, Moens CB, Yu G, Kucenas S (2021) Met is required for oligodendrocyte progenitor cell migration in Danio rerio. G3 (Bethesda) 11: Doi 10.1093/g3journal/jkab265

5 Anfray A, Brodin C, Drieu A, Potzeha F, Dalarun B, Agin V, Vivien D, Orset C (2021) Single- and two- chain tissue type plasminogen activator treatments differentially influence cerebral recovery after stroke. Exp Neurol 338: 113606 Doi 10.1016/j.expneurol.2021.113606

6 Badia IMP, Vélez Santiago J, Braunger J, Geiss C, Dimitrov D, Müller-Dott S, Taus P, Dugourd A, Holland CH, Ramirez Flores ROet al (2022) decoupleR: ensemble of computational methods to infer biological activities from omics data. Bioinform Adv 2: vbac016 Doi 10.1093/bioadv/vbac016

7 Bai X, Zhao N, Koupourtidou C, Fang LP, Schwarz V, Caudal LC, Zhao R, Hirrlinger J, Walz W, Bian Set al (2023) In the mouse cortex, oligodendrocytes regain a plastic capacity, transforming into astrocytes after acute injury. Dev Cell 58: 1153-1169.e1155 Doi 10.1016/j.devcel.2023.04.016

8 Bankhead P, Loughrey MB, Fernández JA, Dombrowski Y, McArt DG, Dunne PD, McQuaid S, Gray RT, Murray LJ, Coleman HGet al (2017) QuPath: Open source software for digital pathology image analysis. Sci Rep 7: 16878 Doi 10.1038/s41598-017-17204-5

9 Bernhardt J, Hayward KS, Kwakkel G, Ward NS, Wolf SL, Borschmann K, Krakauer JW, Boyd LA, Carmichael ST, Corbett Det al (2017) Agreed definitions and a shared vision for new standards in stroke recovery research: The Stroke Recovery and Rehabilitation Roundtable taskforce. Int J Stroke 12: 444-450 Doi 10.1177/1747493017711816

10 Beuker C, Schafflick D, Strecker JK, Heming M, Li X, Wolbert J, Schmidt-Pogoda A, Thomas C, Kuhlmann T, Aranda-Pardos Iet al (2022) Stroke induces disease-specific myeloid cells in the brain parenchyma and pia. Nat Commun 13: 945 Doi 10.1038/s41467-022-28593-1

11 Blanco-Carmona E (2022) Generating publication ready visualizations for Single Cell transcriptomics using SCpubr. bioRxiv: 2022.2002.2028.482303 Doi 10.1101/2022.02.28.482303

12 Blighe K, Rana S, Lewis M (2019) EnhancedVolcano: Publication-ready volcano plots with enhanced colouring and labeling. R package version 1:

13 Boghdadi AG, Spurrier J, Teo L, Li M, Skarica M, Cao B, Kwan WC, Merson TD, Nilsson SK, Sestan Net al (2021) NogoA-expressing astrocytes limit peripheral macrophage infiltration after ischemic brain injury in primates. Nat Commun 12: 6906 Doi 10.1038/s41467-021-27245-0

14 Bonfanti E, Gelosa P, Fumagalli M, Dimou L, Viganò F, Tremoli E, Cimino M, Sironi L, Abbracchio MP (2017) The role of oligodendrocyte precursor cells expressing the GPR17 receptor in brain remodeling after stroke. Cell Death Dis 8: e2871 Doi 10.1038/cddis.2017.256

15 Bormann D, Copic D, Klas K, Direder M, Riedl CJ, Testa G, Kühtreiber H, Poreba E, Hametner S, Golabi Bet al (2023) Exploring the heterogeneous transcriptional response of the CNS to systemic LPS and Poly(I:C). Neurobiol Dis 188: 106339 Doi 10.1016/j.nbd.2023.106339

16 Buizza C, Enström A, Carlsson R, Paul G (2023) The Transcriptional Landscape of Pericytes in Acute Ischemic Stroke. Transl Stroke Res: Doi 10.1007/s12975-023-01169-x

17 Campbell BCV, De Silva DA, Macleod MR, Coutts SB, Schwamm LH, Davis SM, Donnan GA (2019) Ischaemic stroke. Nat Rev Dis Primers 5: 70 Doi 10.1038/s41572-019-0118-8

18 Cao J, Spielmann M, Qiu X, Huang X, Ibrahim DM, Hill AJ, Zhang F, Mundlos S, Christiansen L, Steemers FJet al (2019) The single-cell transcriptional landscape of mammalian organogenesis. Nature 566: 496-502 Doi 10.1038/s41586-019-0969-x

19 Carulli D, de Winter F, Verhaagen J (2021) Semaphorins in Adult Nervous System Plasticity and Disease. Front Synaptic Neurosci 13: 672891 Doi 10.3389/fnsyn.2021.672891

20 Cassidy JM, Cramer SC (2017) Spontaneous and Therapeutic-Induced Mechanisms of Functional Recovery After Stroke. Transl Stroke Res 8: 33-46 Doi 10.1007/s12975-016-0467-5

21 Choudhary S, Satija R (2022) Comparison and evaluation of statistical error models for scRNA-seq. Genome Biol 23: 27 Doi 10.1186/s13059-021-02584-9

22 Conway JR, Lex A, Gehlenborg N (2017) UpSetR: an R package for the visualization of intersecting sets and their properties. Bioinformatics 33: 2938-2940 Doi 10.1093/bioinformatics/btx364

23 Cregg JM, DePaul MA, Filous AR, Lang BT, Tran A, Silver J (2014) Functional regeneration beyond the glial scar. Exp Neurol 253: 197-207 Doi 10.1016/j.expneurol.2013.12.024

24 Dai J, Bercury KK, Ahrendsen JT, Macklin WB (2015) Olig1 function is required for oligodendrocyte differentiation in the mouse brain. J Neurosci 35: 4386-4402 Doi 10.1523/jneurosci.4962-14.2015

25 Daniele SG, Trummer G, Hossmann KA, Vrselja Z, Benk C, Gobeske KT, Damjanovic D, Andrijevic D, Pooth JS, Dellal Det al (2021) Brain vulnerability and viability after ischaemia. Nat Rev Neurosci 22: 553-572 Doi 10.1038/s41583-021-00488-y

26 Dimitrov D, Türei D, Garrido-Rodriguez M, Burmedi PL, Nagai JS, Boys C, Ramirez Flores RO, Kim H, Szalai B, Costa IGet al (2022) Comparison of methods and resources for cell-cell communication inference from single-cell RNA-Seq data. Nat Commun 13: 3224 Doi 10.1038/s41467-022-30755-0

27 Dzwonek J, Wilczynski GM (2015) CD44: molecular interactions, signaling and functions in the nervous system. Front Cell Neurosci 9: 175 Doi 10.3389/fncel.2015.00175

28 Fan J, Li X, Yu X, Liu Z, Jiang Y, Fang Y, Zong M, Suo C, Man Q, Xiong L (2023) Global Burden, Risk Factor Analysis, and Prediction Study of Ischemic Stroke, 1990-2030. Neurology 101: e137-e150 Doi 10.1212/wnl.0000000000207387

29 Fard MK, van der Meer F, Sánchez P, Cantuti-Castelvetri L, Mandad S, Jäkel S, Fornasiero EF, Schmitt S, Ehrlich M, Starost Let al (2017) BCAS1 expression defines a population of early myelinating oligodendrocytes in multiple sclerosis lesions. Sci Transl Med 9: Doi 10.1126/scitranslmed.aam7816

30 Finak G, McDavid A, Yajima M, Deng J, Gersuk V, Shalek AK, Slichter CK, Miller HW, McElrath MJ, Prlic Met al (2015) MAST: a flexible statistical framework for assessing transcriptional changes and characterizing heterogeneity in single-cell RNA sequencing data. Genome Biol 16: 278 Doi 10.1186/s13059-015-0844-5

31 Fulda S, Gorman AM, Hori O, Samali A (2010) Cellular stress responses: cell survival and cell death. Int J Cell Biol 2010: 214074 Doi 10.1155/2010/214074

32 Gadani SP, Walsh JT, Smirnov I, Zheng J, Kipnis J (2015) The glia-derived alarmin IL-33 orchestrates the immune response and promotes recovery following CNS injury. Neuron 85: 703-709 Doi 10.1016/j.neuron.2015.01.013

33 Gliem M, Krammes K, Liaw L, van Rooijen N, Hartung HP, Jander S (2015) Macrophage-derived osteopontin induces reactive astrocyte polarization and promotes re-establishment of the blood brain barrier after ischemic stroke. Glia 63: 2198-2207 Doi 10.1002/glia.22885

34 Gu Z, Eils R, Schlesner M (2016) Complex heatmaps reveal patterns and correlations in multidimensional genomic data. Bioinformatics 32: 2847-2849 Doi 10.1093/bioinformatics/btw313

35 Guo K, Luo J, Feng D, Wu L, Wang X, Xia L, Tao K, Wu X, Cui W, He Yet al (2021) Single-Cell RNA Sequencing With Combined Use of Bulk RNA Sequencing to Reveal Cell Heterogeneity

and Molecular Changes at Acute Stage of Ischemic Stroke in Mouse Cortex Penumbra Area. Front Cell Dev Biol 9: 624711 Doi 10.3389/fcell.2021.624711

36 Habib N, McCabe C, Medina S, Varshavsky M, Kitsberg D, Dvir-Szternfeld R, Green G, Dionne D, Nguyen L, Marshall JLet al (2020) Disease-associated astrocytes in Alzheimer's disease and aging. Nat Neurosci 23: 701-706 Doi 10.1038/s41593-020-0624-8

37 Hafemeister C, Satija R (2019) Normalization and variance stabilization of single-cell RNA-seq data using regularized negative binomial regression. Genome Biol 20: 296 Doi 10.1186/s13059-019-1874-1

38 Hammond TR, Dufort C, Dissing-Olesen L, Giera S, Young A, Wysoker A, Walker AJ, Gergits F, Segel M, Nemesh Jet al (2019) Single-Cell RNA Sequencing of Microglia throughout the Mouse Lifespan and in the Injured Brain Reveals Complex Cell-State Changes. Immunity 50: 253-271.e256 Doi 10.1016/j.immuni.2018.11.004

39 Hao Y, Hao S, Andersen-Nissen E, Mauck WM, 3rd, Zheng S, Butler A, Lee MJ, Wilk AJ, Darby C, Zager Met al (2021) Integrated analysis of multimodal single-cell data. Cell 184: 3573-3587.e3529 Doi 10.1016/j.cell.2021.04.048

40 Herrmann JE, Imura T, Song B, Qi J, Ao Y, Nguyen TK, Korsak RA, Takeda K, Akira S, Sofroniew MV (2008) STAT3 is a critical regulator of astrogliosis and scar formation after spinal cord injury. J Neurosci 28: 7231-7243 Doi 10.1523/jneurosci.1709-08.2008

41 Hu YH, Zhang Y, Jiang LQ, Wang S, Lei CQ, Sun MS, Shu HB, Liu Y (2015) WDFY1 mediates TLR3/4 signaling by recruiting TRIF. EMBO Rep 16: 447-455 Doi 10.15252/embr.201439637

42 Huang JK, Jarjour AA, Nait Oumesmar B, Kerninon C, Williams A, Krezel W, Kagechika H, Bauer J, Zhao C, Baron-Van Evercooren Aet al (2011) Retinoid X receptor gamma signaling accelerates CNS remyelination. Nat Neurosci 14: 45-53 Doi 10.1038/nn.2702

43 Huang S, Ren C, Luo Y, Ding Y, Ji X, Li S (2023) New insights into the roles of oligodendrocytes regulation in ischemic stroke recovery. Neurobiol Dis 184: 106200 Doi 10.1016/j.nbd.2023.106200

44 Ignatenko O, Malinen S, Rybas S, Vihinen H, Nikkanen J, Kononov A, Jokitalo ES, Ince-Dunn G, Suomalainen A (2023) Mitochondrial dysfunction compromises ciliary homeostasis in astrocytes. J Cell Biol 222: Doi 10.1083/jcb.202203019

45 Jin C, Shi Y, Shi L, Leak RK, Zhang W, Chen K, Ye Q, Hassan S, Lyu J, Hu Xet al (2023) Leveraging single-cell RNA sequencing to unravel the impact of aging on stroke recovery mechanisms in mice. Proc Natl Acad Sci U S A 120: e2300012120 Doi 10.1073/pnas.2300012120

46 Kanda A, Noda K, Hirose I, Ishida S (2019) TGF-β-SNAIL axis induces Müller glial-mesenchymal transition in the pathogenesis of idiopathic epiretinal membrane. Sci Rep 9: 673 Doi 10.1038/s41598-018-36917-9

47 Kaneko N, Herranz-Pérez V, Otsuka T, Sano H, Ohno N, Omata T, Nguyen HB, Thai TQ, Nambu A, Kawaguchi Yet al (2018) New neurons use Slit-Robo signaling to migrate through the glial meshwork and approach a lesion for functional regeneration. Sci Adv 4: eaav0618 Doi 10.1126/sciadv.aav0618

48 Kenigsbuch M, Bost P, Halevi S, Chang Y, Chen S, Ma Q, Hajbi R, Schwikowski B, Bodenmiller B, Fu Het al (2022) A shared disease-associated oligodendrocyte signature among multiple CNS pathologies. Nat Neurosci 25: 876-886 Doi 10.1038/s41593-022-01104-7

49 Kim S, Lee W, Jo H, Sonn SK, Jeong SJ, Seo S, Suh J, Jin J, Kweon HY, Kim TKet al (2022) The antioxidant enzyme Peroxiredoxin-1 controls stroke-associated microglia against acute ischemic stroke. Redox Biol 54: 102347 Doi 10.1016/j.redox.2022.102347

50 Kirdajova D, Valihrach L, Valny M, Kriska J, Krocianova D, Benesova S, Abaffy P, Zucha D, Klassen R, Kolenicova Det al (2021) Transient astrocyte-like NG2 glia subpopulation emerges solely following permanent brain ischemia. Glia 69: 2658-2681 Doi 10.1002/glia.24064

51 Kolberg L, Raudvere U, Kuzmin I, Vilo J, Peterson H (2020) gprofiler2 -- an R package for gene list functional enrichment analysis and namespace conversion toolset g:Profiler. F1000Res 9: Doi 10.12688/f1000research.24956.2

52 Kolde R (2012) Pheatmap: pretty heatmaps. R package version 1: 726

53 Kolonko M, Greb-Markiewicz B (2019) bHLH-PAS Proteins: Their Structure and Intrinsic Disorder. Int J Mol Sci 20: Doi 10.3390/ijms20153653

54 Krämer-Albers EM, White R (2011) From axon-glial signalling to myelination: the integrating role of oligodendroglial Fyn kinase. Cell Mol Life Sci 68: 2003-2012 Doi 10.1007/s00018-010-0616-z

55 Kuleshov MV, Jones MR, Rouillard AD, Fernandez NF, Duan Q, Wang Z, Koplev S, Jenkins SL, Jagodnik KM, Lachmann Aet al (2016) Enrichr: a comprehensive gene set enrichment analysis web server 2016 update. Nucleic Acids Res 44: W90-97 Doi 10.1093/nar/gkw377

56 Lee MN, Song JH, Oh SH, Tham NT, Kim JW, Yang JW, Kim ES, Koh JT (2020) The primary cilium directs osteopontin-induced migration of mesenchymal stem cells by regulating CD44 signaling and Cdc42 activation. Stem Cell Res 45: 101799 Doi 10.1016/j.scr.2020.101799

57 Lein ES, Hawrylycz MJ, Ao N, Ayres M, Bensinger A, Bernard A, Boe AF, Boguski MS, Brockway KS, Byrnes EJet al (2007) Genome-wide atlas of gene expression in the adult mouse brain. Nature 445: 168-176 Doi 10.1038/nature05453

58 Li X, Lyu J, Li R, Jain V, Shen Y, Del Águila Á, Hoffmann U, Sheng H, Yang W (2022) Single-cell transcriptomic analysis of the immune cell landscape in the aged mouse brain after ischemic stroke. J Neuroinflammation 19: 83 Doi 10.1186/s12974-022-02447-5

59 Liddelow SA, Guttenplan KA, Clarke LE, Bennett FC, Bohlen CJ, Schirmer L, Bennett ML, Münch AE, Chung WS, Peterson TCet al (2017) Neurotoxic reactive astrocytes are induced by activated microglia. Nature 541: 481-487 Doi 10.1038/nature21029

60 Liu X, Hu R, Pei L, Si P, Wang C, Tian X, Wang X, Liu H, Wang B, Xia Zet al (2020) Regulatory T cell is critical for interleukin-33-mediated neuroprotection against stroke. Exp Neurol 328: 113233 Doi 10.1016/j.expneurol.2020.113233

61 Lv Y, Zhang B, Zhai C, Qiu J, Zhang Y, Yao W, Zhang C (2015) PFKFB3-mediated glycolysis is involved in reactive astrocyte proliferation after oxygen-glucose deprivation/reperfusion and is regulated by Cdh1. Neurochem Int 91: 26-33 Doi 10.1016/j.neuint.2015.10.006

62 Maitra M, Nagy C, Chawla A, Wang YC, Nascimento C, Suderman M, Théroux JF, Mechawar N, Ragoussis J, Turecki G (2021) Extraction of nuclei from archived postmortem tissues for single-nucleus sequencing applications. Nat Protoc 16: 2788-2801 Doi 10.1038/s41596-021-00514-4

63 Marsh SE (2021) scCustomize: Custom Visualizations & Functions for Streamlined Analyses of Single Cell Sequencing. . v.1.1.1 https://doi.org/10.5281/zenodo.5706430. RRID:SCR_024675. edn, City

64 Matsumura I, Tanaka H, Kanakura Y (2003) E2F1 and c-Myc in cell growth and death. Cell Cycle 2: 333-338

65 Matusova Z, Hol EM, Pekny M, Kubista M, Valihrach L (2023) Reactive astrogliosis in the era of single-cell transcriptomics. Front Cell Neurosci 17: 1173200 Doi 10.3389/fncel.2023.1173200

66 McGinnis CS, Murrow LM, Gartner ZJ (2019) DoubletFinder: Doublet Detection in Single-Cell RNA Sequencing Data Using Artificial Nearest Neighbors. Cell Syst 8: 329-337.e324 Doi 10.1016/j.cels.2019.03.003

67 Mena H, Cadavid D, Rushing EJ (2004) Human cerebral infarct: a proposed histopathologic classification based on 137 cases. Acta Neuropathol 108: 524-530 Doi 10.1007/s00401-004-0918-z

68 Micu I, Plemel JR, Caprariello AV, Nave KA, Stys PK (2018) Axo-myelinic neurotransmission: a novel mode of cell signalling in the central nervous system. Nat Rev Neurosci 19: 49-58 Doi 10.1038/nrn.2017.128

69 Morris R, Kershaw NJ, Babon JJ (2018) The molecular details of cytokine signaling via the JAK/STAT pathway. Protein Sci 27: 1984-2009 Doi 10.1002/pro.3519

70 Neely SA, Williamson JM, Klingseisen A, Zoupi L, Early JJ, Williams A, Lyons DA (2022) New oligodendrocytes exhibit more abundant and accurate myelin regeneration than those that survive demyelination. Nat Neurosci 25: 415-420 Doi 10.1038/s41593-021-01009-x

71 Noritake J, Watanabe T, Sato K, Wang S, Kaibuchi K (2005) IQGAP1: a key regulator of adhesion and migration. J Cell Sci 118: 2085-2092 Doi 10.1242/jcs.02379

72 Padamsey Z, Rochefort NL (2023) Paying the brain's energy bill. Curr Opin Neurobiol 78: 102668 Doi 10.1016/j.conb.2022.102668

73 Pandey S, Shen K, Lee SH, Shen YA, Wang Y, Otero-García M, Kotova N, Vito ST, Laufer BI, Newton DFet al (2022) Disease-associated oligodendrocyte responses across neurodegenerative diseases. Cell Rep 40: 111189 Doi 10.1016/j.celrep.2022.111189

74 Piao JH, Wang Y, Duncan ID (2013) CD44 is required for the migration of transplanted oligodendrocyte progenitor cells to focal inflammatory demyelinating lesions in the spinal cord. Glia 61: 361-367 Doi 10.1002/glia.22438

75 Piwecka M, Rajewsky N, Rybak-Wolf A (2023) Single-cell and spatial transcriptomics: deciphering brain complexity in health and disease. Nat Rev Neurol 19: 346-362 Doi 10.1038/s41582-023-00809-y

76 Powers WJ, Rabinstein AA, Ackerson T, Adeoye OM, Bambakidis NC, Becker K, Biller J, Brown M, Demaerschalk BM, Hoh Bet al (2019) Guidelines for the Early Management of Patients With Acute Ischemic Stroke: 2019 Update to the 2018 Guidelines for the Early Management of Acute Ischemic Stroke: A Guideline for Healthcare Professionals From the American Heart Association/American Stroke Association. Stroke 50: e344-e418 Doi 10.1161/str.0000000000000211

77 Qi Y, Cai J, Wu Y, Wu R, Lee J, Fu H, Rao M, Sussel L, Rubenstein J, Qiu M (2001) Control of oligodendrocyte differentiation by the Nkx2.2 homeodomain transcription factor. Development 128: 2723-2733 Doi 10.1242/dev.128.14.2723

78 Qian Z, Qin J, Lai Y, Zhang C, Zhang X (2023) Large-Scale Integration of Single-Cell RNA-Seq Data Reveals Astrocyte Diversity and Transcriptomic Modules across Six Central Nervous System Disorders. Biomolecules 13: Doi 10.3390/biom13040692

79 Qin C, Yang S, Chu YH, Zhang H, Pang XW, Chen L, Zhou LQ, Chen M, Tian DS, Wang W (2022) Signaling pathways involved in ischemic stroke: molecular mechanisms and therapeutic interventions. Signal Transduct Target Ther 7: 215 Doi 10.1038/s41392-022-01064-1

80 Rakers C, Schleif M, Blank N, Matušková H, Ulas T, Händler K, Torres SV, Schumacher T, Tai K, Schultze JLet al (2019) Stroke target identification guided by astrocyte transcriptome analysis. Glia 67: 619-633 Doi 10.1002/glia.23544

81 Ruediger T, Zimmer G, Barchmann S, Castellani V, Bagnard D, Bolz J (2013) Integration of opposing semaphorin guidance cues in cortical axons. Cereb Cortex 23: 604-614 Doi 10.1093/cercor/bhs044

82 Sakai S, Shichita T (2019) Inflammation and neural repair after ischemic brain injury. Neurochem Int 130: 104316 Doi 10.1016/j.neuint.2018.10.013

83 Sawada R, Nakano-Doi A, Matsuyama T, Nakagomi N, Nakagomi T (2020) CD44 expression in stem cells and niche microglia/macrophages following ischemic stroke. Stem Cell Investig 7: 4 Doi 10.21037/sci.2020.02.02

84 Schirmer L, Velmeshev D, Holmqvist S, Kaufmann M, Werneburg S, Jung D, Vistnes S, Stockley JH, Young A, Steindel Met al (2019) Neuronal vulnerability and multilineage diversity in multiple sclerosis. Nature 573: 75-82 Doi 10.1038/s41586-019-1404-z

85 Shankar SL, O'Guin K, Kim M, Varnum B, Lemke G, Brosnan CF, Shafit-Zagardo B (2006) Gas6/Axl signaling activates the phosphatidylinositol 3-kinase/Akt1 survival pathway to protect oligodendrocytes from tumor necrosis factor alpha-induced apoptosis. J Neurosci 26: 5638-5648 Doi 10.1523/jneurosci.5063-05.2006

86 Shen XY, Gao ZK, Han Y, Yuan M, Guo YS, Bi X (2021) Activation and Role of Astrocytes in Ischemic Stroke. Front Cell Neurosci 15: 755955 Doi 10.3389/fncel.2021.755955

87 Shi L, Sun Z, Su W, Xu F, Xie D, Zhang Q, Dai X, Iyer K, Hitchens TK, Foley LMet al (2021) Treg cell-derived osteopontin promotes microglia-mediated white matter repair after ischemic stroke. Immunity 54: 1527-1542.e1528 Doi 10.1016/j.immuni.2021.04.022

88 Shin SY, Song H, Kim CG, Choi YK, Lee KS, Lee SJ, Lee HJ, Lim Y, Lee YH (2009) Egr-1 is necessary for fibroblast growth factor-2-induced transcriptional activation of the glial cell line-derived neurotrophic factor in murine astrocytes. J Biol Chem 284: 30583-30593 Doi 10.1074/jbc.M109.010678

89 Silvin A, Uderhardt S, Piot C, Da Mesquita S, Yang K, Geirsdottir L, Mulder K, Eyal D, Liu Z, Bridlance Cet al (2022) Dual ontogeny of disease-associated microglia and disease inflammatory macrophages in aging and neurodegeneration. Immunity 55: 1448-1465.e1446 Doi 10.1016/j.immuni.2022.07.004

90 Spitzer D, Guérit S, Puetz T, Khel MI, Armbrust M, Dunst M, Macas J, Zinke J, Devraj G, Jia Xet al (2022) Profiling the neurovascular unit unveils detrimental effects of osteopontin on the blood-brain barrier in acute ischemic stroke. Acta Neuropathol 144: 305-337 Doi 10.1007/s00401-022-02452-1

91 Steelman AJ, Zhou Y, Koito H, Kim S, Payne HR, Lu QR, Li J (2016) Activation of oligodendroglial Stat3 is required for efficient remyelination. Neurobiol Dis 91: 336-346 Doi 10.1016/j.nbd.2016.03.023

92 Sung HY, Chen WY, Huang HT, Wang CY, Chang SB, Tzeng SF (2019) Down-regulation of interleukin-33 expression in oligodendrocyte precursor cells impairs oligodendrocyte lineage progression. J Neurochem 150: 691-708 Doi 10.1111/jnc.14788

93 Trapnell C, Cacchiarelli D, Grimsby J, Pokharel P, Li S, Morse M, Lennon NJ, Livak KJ, Mikkelsen TS, Rinn JL (2014) The dynamics and regulators of cell fate decisions are revealed by pseudotemporal ordering of single cells. Nat Biotechnol 32: 381-386 Doi 10.1038/nbt.2859

94 Türei D, Valdeolivas A, Gul L, Palacio-Escat N, Klein M, Ivanova O, Ölbei M, Gábor A, Theis F, Módos Det al (2021) Integrated intra- and intercellular signaling knowledge for multicellular omics analysis. Mol Syst Biol 17: e9923 Doi 10.15252/msb.20209923

95 Vay SU, Olschewski DN, Petereit H, Lange F, Nazarzadeh N, Gross E, Rabenstein M, Blaschke SJ, Fink GR, Schroeter Met al (2021) Osteopontin regulates proliferation, migration, and survival of astrocytes depending on their activation phenotype. J Neurosci Res 99: 2822-2843 Doi 10.1002/jnr.24954

96 Verkhratsky A, Nedergaard M (2018) Physiology of Astroglia. Physiol Rev 98: 239-389 Doi 10.1152/physrev.00042.2016

97 Wei H, Wu X, Withrow J, Cuevas-Diaz Duran R, Singh S, Chaboub LS, Rakshit J, Mejia J, Rolfe A, Herrera JJet al (2023) Glial progenitor heterogeneity and key regulators revealed by single-cell RNA sequencing provide insight to regeneration in spinal cord injury. Cell Rep 42: 112486 Doi 10.1016/j.celrep.2023.112486

98 Wickham H (2016) Data Analysis. In: Wickham H (ed) ggplot2: Elegant Graphics for Data Analysis. Springer International Publishing, City, pp 189-201

99 Xiao Y, Czopka T (2023) Myelination-independent functions of oligodendrocyte precursor cells in health and disease. Nat Neurosci 26: 1663-1669 Doi 10.1038/s41593-023-01423-3

100 Xie D, Liu H, Xu F, Su W, Ye Q, Yu F, Austin TJ, Chen J, Hu X (2021) IL33 (Interleukin 33)/ST2 (Interleukin 1 Receptor-Like 1) Axis Drives Protective Microglial Responses and Promotes White Matter Integrity After Stroke. Stroke 52: 2150-2161 Doi 10.1161/strokeaha.120.032444

101 Xu S, Lu J, Shao A, Zhang JH, Zhang J (2020) Glial Cells: Role of the Immune Response in Ischemic Stroke. Front Immunol 11: 294 Doi 10.3389/fimmu.2020.00294

102 Young MD, Behjati S (2020) SoupX removes ambient RNA contamination from droplet-based single-cell RNA sequencing data. Gigascience 9: Doi 10.1093/gigascience/giaa151

103 Zamanian JL, Xu L, Foo LC, Nouri N, Zhou L, Giffard RG, Barres BA (2012) Genomic analysis of reactive astrogliosis. J Neurosci 32: 6391-6410 Doi 10.1523/jneurosci.6221-11.2012

104 Zeisel A, Hochgerner H, Lönnerberg P, Johnsson A, Memic F, van der Zwan J, Häring M, Braun E, Borm LE, La Manno Get al (2018) Molecular Architecture of the Mouse Nervous System. Cell 174: 999-1014.e1022 Doi 10.1016/j.cell.2018.06.021

105 Zheng K, Lin L, Jiang W, Chen L, Zhang X, Zhang Q, Ren Y, Hao J (2022) Single-cell RNA-seq reveals the transcriptional landscape in ischemic stroke. J Cereb Blood Flow Metab 42: 56-73 Doi 10.1177/0271678x211026770

106 Zou C, Luo Q, Qin J, Shi Y, Yang L, Ju B, Song G (2013) Osteopontin promotes mesenchymal stem cell migration and lessens cell stiffness via integrin β1, FAK, and ERK pathways. Cell Biochem Biophys 65: 455-462 Doi 10.1007/s12013-012-9449-8

Data availability statement

Single nucleus RNA-seq datasets reported in the present paper will be made publicly available via the NCBI-GEO database, after completion of peer review and publication. All other raw data supporting the herein made conclusions is available upon reasonable request.

Funding

This work was supported by the Austrian Research Promotion Agency (#852748, #862068), the Vienna Business Agency (#2343727) and the Aposcience AG. This study was also supported by VASCage – Centre on Clinical Stroke Research. VASCage is a COMET Centre within the Competence Centers for Excellent Technologies (COMET) programme and funded by the Federal Ministry for Climate Action, Environment, Energy, Mobility, Innovation and Technology, the Federal Ministry of Labour and Economy, and the federal states of Tyrol, Salzburg and Vienna. COMET is managed by the Austrian Research Promotion Agency (Österreichische Forschungsförderungsgesellschaft) - FFG Project number: 898252. SH gratefully acknowledges funding by the National Institutes of Health (1R01NS114227-01A1 to SH). SzN and GBB were supported by the Austrian Science Fund (FWF), grant numbers T1091, P31085-B26.

Conflict of interest

The authors declare that the research has been performed without any conflict of interest.

Author contributions

DB and MM: conceptualization – overall design of the study. DB, MK, CO, SzN, GBB, SK, HJA, MM: conceptualization/methodology – design of *in vivo* experiments, sample acquisition and general analysis strategy. CO, AL, AC: investigation – execution of *in vivo* MCAO and MRI experiments. DB, DC, KK, MD: investigation – scRNAseq experiments. DB, EP, CJR, GT, PJ, BG, HK, MS, CH, VE: investigation – immunofluorescence staining experiments. DB, CJR, GT, HK, MS: investigation – cell culture experiments. DB, MK, CO, AL, AC, SzN, GBB, SK: formal analysis/data curation – MRI data. DB, EP, CJR, PJ, SH, RH, MM: formal analysis/data curation – immunofluorescence staining and cell culture data. DB: formal analysis and data curation – bioinformatics analyses. DB, DC, KK, MD: data curation/validation - bioinformatics analyses. HJA, MM: funding acquisition. HJA, MM: project

administration. CO, SH, SK, RH, HJA, MM: resources. RH, SH, HJA, MM: supervision – HJA and MM supervised DB, RH and SH supervised CJR, GT, VE, CH. DB and MM: writing – original draft, visualization. All authors were involved in review & editing and approved of the final manuscript.

Acknowledgment

We would like to thank Hans Peter Haselsteiner and the CRISCAR Familienstiftung for their ongoing support of the Medical University/Aposcience AG public private partnership aiming to augment basic and translational clinical research in Austria/Europe. The authors acknowledge the core facilities of the Medical University of Vienna, a member of Vienna Life Science Instruments. We also thank Matthias Wielscher for his support in bioinformatics analyses and Irene Erber and the team of Matthias Farlik-Födinger for their invaluable technical support.